Splashing by laser ablation of a liquid tin layer on a solid substrate

an investigation of substrate geometry effect on thin film splashing and an analysis of secondary droplet commutability between droplet and laser impact

Duffhues, J.C.J.

Award date:
2020

Splashing by laser ablation of a liquid tin layer on a solid substrate

An investigation of substrate geometry effect on thin film splashing and an analysis of secondary droplet commutability between droplet and laser impact.

Supervised by dr. O.O. Versolato, dr. P. Rindt, and dr. prof. N. Lopes Cardozo

J.C.J. Duffhues 0816765

April 5, 2020

ARCNL
ADVANCED RESEARCH CENTER FOR NANOLITHOGRAPHY

TU/e EINDHOVEN UNIVERSITY OF TECHNOLOGY

Abstract

In today's world the demand for computational capacity is rising. To meet this demand, nanolithography, a method of printing on the nano scale, is rushing to lower wavelength light sources. The lower wavelength of the light allows for smaller objects to be printed and computer chips to increase in potential without increasing in size. One of the problems of generating low wavelength light is the availability of the extreme ultra violet (EUV) emitting tin plasma. At ASML a mass limited target is used, this method uses a continuous stream of tiny tin droplets being ablated mid flight by a laser. One of the drawbacks of this method is the instability and short lifetime of the droplet dispenser. To circumvent this problem an alternative light source is investigated. This alternative source uses the concept of a porous substrate with a liquid metal layer on top from liquid metal divertors from fusion.

A liquid tin layer is deposited on a solid tungsten substrate, this liquid is hit with a laser creating a tin plasma emitting low wavelength light. However, after the formation of the plasma, a splash of the liquid is observed. An investigation into the effect of the target geometry and analysis of the secondary droplets is performed in this work. To do this, a Nd:YAG 1064nm wavelength laser with variable laser energy and spot size is used. A target, held in place by a target holder, is impacted with the laser. The resulting splash from laser impact is captured using a CCD camera and a back light, creating a 2D image.

In this work experimentation of laser impact on thin and thick liquid tin films on a tungsten substrate is done. The first part is focused on the effect of the substrate surface roughness and geometry on the splash characteristics. The aim of the first part is to suppress the splash by laser impact. The shape, direction, and size of the resulting crown by plasma expansion of a laser produced plasma is observed to change due to spatial location of the laser impact spot on a target. A steerability of the splash is seen in narrow deep baths. Spatially, the geometry of the target is changed due to a micro pattern present on the target surface. This geometry effect is observed for thin liquid films. However, no suppression of the splash is observed.

The second part is focused on the secondary droplet formation on thick liquid layers. The aim of the second part is to understand the secondary droplet generation of the laser impact splash and investigate its commutability with the droplet impact splash. The secondary droplets resulting from laser impact are gathered into droplet diameter distributions and compared to literature of droplet impact secondary droplet diameter distributions. A relation of $We^{-1/4}$ for the rim diameter of the laser impact case is found for the secondary droplet diameter. For higher input energy, the droplet distribution is narrow and centered around lower droplet diameters for the initial distribution. For lower input energy, the droplet distribution is broad and centered around higher droplet diameters for the initial distribution. Furthermore, evidence for prompt splashing and delayed splashing mechanisms are found in laser impact splashing by agreeable fitting of a Gauss curve from literature on the distributions in late time stages of the splash. In conclusion, commutability between the droplet and laser impact splashing is strongly suspected.

Contents

1 Introduction

The modern period of electronic devices shows a trend towards a higher computational capacity. As recent developments allowed progress to be made in mobile networks, virtual and enhanced reality, and of course simulations, the demand for more powerful computers to support these developments is rising. To accommodate this trend, the chip manufacturing industry searches for ways to accurately produce smaller and more complex chip structures.

Recent developments in the field of lithography use light in the extreme ultraviolet (EUV) range to expose a pattern to a substrate. The process uses light to change the solubility of the chip after which the chip is etched and the exposed structure is embedded into the chip. This lithography process is graphically depicted in figure 1.1. As the sizes of these patterns continue to decrease, the wavelengths of the UV light must decrease as well in order to allow for smaller features following the Abbe limit given in equation 1. With s the smallest resolvable distance, λ the wavelength of the light, and NA the numerical aperture.

$$s = \frac{\lambda}{2NA} \tag{1}$$

This development to smaller wavelengths is an ongoing quest in nanolithography. The previous method, and the most used lithography machines, use deep ultraviolet (DUV) light in the range of 150nm-180nm to remove a photo resist (PR) layer. In a recent breakthrough the wavelength of the light used in nanolithography is shifted from DUV to EUV light with a wavelength of 13.5nm. The large gap between DUV and EUV light wavelength is due to the rarity of light sources between 150nm and 20nm. No stable and readily available source is at hand [1]. The source for the 13.5nm EUV light is a high energy tin plasma, this particular wavelength is chosen as the standard wavelength for ASML's EUV nanolithography machines.

Currently the light with a wavelength of 13.5nm is generated by tin plasmas inside the lithography machine by ablating a tin droplet midflight, as seen in figure 1.2. Research into the generation and optimization of extreme ultra violet (EUV) light is ongoing [2, 3].

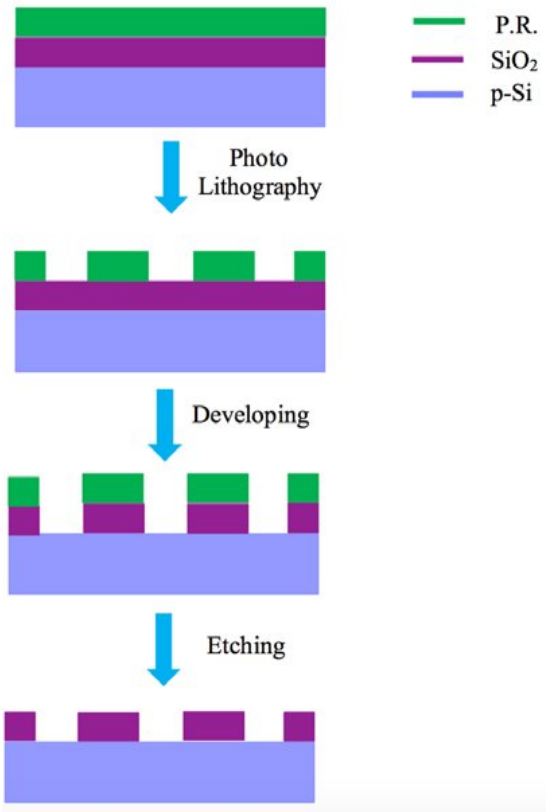

Figure 1.1: A schematic figure of the lithography process. In the first step a silicon wafer (gray) with an oxide layer (purple) is topped with photoresist (green). After exposure to UV light the photoresist layer is locally removed. Development will remove the oxide layer at the exposed locations. After development, an etchant removes the rest of the photoresist layer. adopted from [4].

The current method of EUV light generation uses small tin droplets, called mass-limited targets, hit by a pre-pulse to flatten them and subsequently ablating the pancake with the main pulse midflight. This generates a tin plasma, which emits a spectrum of light, including the desired 13.5nm light. The main reason of using mass-limited targets is the exposure of the optical elements to the debris from the laser ablation, as this exposure will lead to damage on the mirrors and reduced transmission. By creating a tiny droplet as a target and ablating the entire target, only minimal debris can be deposited on the mirrors. One of the technical bottlenecks of the current method is the driving gas pressure and droplet dispenser frequency. The driving gas is used to accelerate the droplets to high speeds, the frequency of the dispenser sets the amount of droplets dispensed per second. Secondly, the droplets must have a sufficiently large inter-droplet spacing to prevent plasma-droplet interaction. An ever increasing droplet velocity is required to meet the demand on an ever increasing inter-droplet spacing, creating a challenge. Not only inter-droplet spacing is subject to strict demands, droplet dispenser frequency and laser frequency too. Commercially, a higher droplet dispenser frequency and laser frequency translates to a higher EUV intensity and exposure yield. The reported size, frequency, and

velocity of tin droplets in an EUV source in 2018 were 27 µm, tens of meters per second, and 50kHz respectively [3]. A droplet velocity of 15m/s requires a pressure of 50 bars [5], which can make the small droplet unstable and influence its shape. The power of the EUV light emitted by the tin plasma must be high, in the range of 50−120W of EUV power at the intermediate focus [5] (see figure 1.2). This intensity must be high as the optical relay system has several mirrors with a reflection ratio of 60−70% [1] and the machine must be able to expose at least 100 wafers per hour, for commercial reasons. In addition, the high dispenser frequency of releasing the droplets may influence the previously dispensed droplet, destabilizing the system. Also, the chance of missing a droplet with the laser pulse will increase with increased droplet velocity and dispenser frequency. Missing droplets will decrease the efficiency of the EUV light generation. The optimization of the lithography process is an important part for any company utilizing nanolithography. Therefore, recently at ARCNL and the fusion group of the TU/e an alternative EUV light source is investigated using developments from fusion energy research.

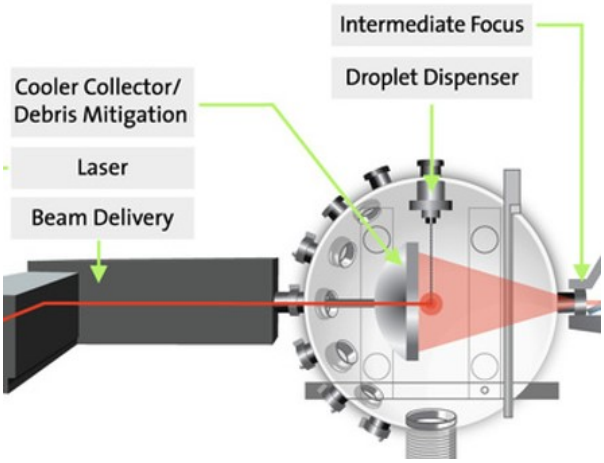

Figure 1.2: A schematic of a nanolithography EUV source, including tin droplet dispenser, laser, and intermediate focus. The inside of the machine is kept under vacuum and a flow of hydrogen buffer gas mitigates debris. The most relevant aspect of the machine for this study is the ablation of the tin droplets by the laser generating the 13.5nm EUV light for nanolithography. adopted from [5].

In fusion research recent developments in plasma facing materials focus on using liquid metal to face the plasma inside a tokamak which can be up to 15 keV [6–9]. A tokamak is an torus shaped magnetic confinement fusion device. The region where this plasma is in contact with the outer wall will experience a problematically large heat flux of 10MW/m^2 in the case of ITER. To resist this large power deposited on the wall, a porous sponge-like structure filled with liquid metal is proposed to absorb this power. The carefully designed capillary pores in the solid structure will distribute the liquid metal over the surface of the porous block. When this block is in contact with the plasma, the liquid metal is evaporated and creates a vapor shield, absorbing energy and consequently radiating this energy away in all directions. This effect allows for higher acceptable heat loads on the block. In addition, the surface tension of the liquid metal discourages it from splashing and forming droplets. For some fusion devices, such as Magnum-PSI and NSTX, the degree of contamination of the plasma from the liquid metal is studied and found to be negligible as most evaporated metal is redeposited onto the block. In addition, splash free shots were observed during operation in Magnum-PSI and NSTX [10, 11] respectively. This lack of splashing is contributed to the small pore size in the solid divertor block [10]. Furthermore, the capillary action distributes new liquid metal to the plasma facing surface after evaporation of the previous layer.

An alternative method of generating the EUV lithography light may use the liquid metal blocks, which are 3D printed, from fusion research. 3D printing allows for a multitude of functional shapes and sizes unobtainable through traditional manufacturing techniques. The specific 13.5nm wavelength emitting plasma can be generated by laser ablating a thin liquid film over a solid tungsten target, creating a tin plasma which emits the EUV light. This technology may be adapted from the liquid metal blocks in the fusion field. However, whereas in a fusion reactor the liquid metal on the block is vaporized and ionized to dissipate the massive energy flux to the walls, in the nanolithography case the liquid metal is vaporized and ionized in order to create a highly specific plasma. Namely, the 13.5nm wavelength light-emitting

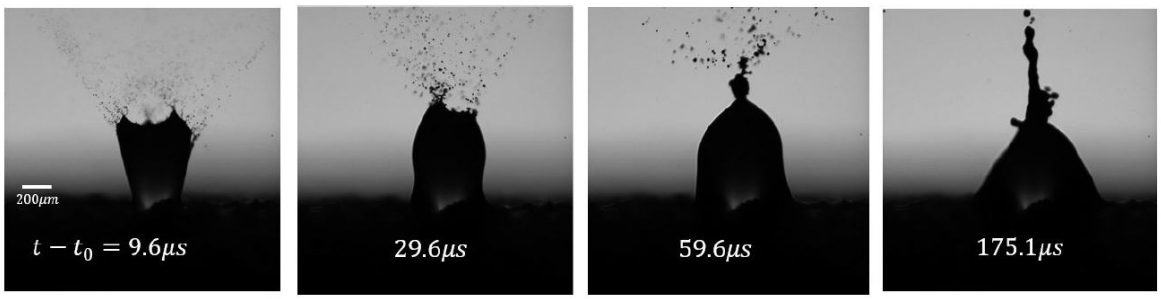

Figure 1.3: The splash caused by laser ablation of the thin tin film over a tungsten target for different times after laser impact. Figures produced using shadowgraphy. Scale is given in the leftmost figure. The layer thickness of the tin is unknown, laser energy is 10mJ for a duration of 0.5ns for a focused beam. As seen the secondary droplet formation throughout, the splash is significant. Courtesy of B.Liu from ARCNL.

tin plasma desired for lithography. By using a non moving tin supply the problems with the fast moving droplets are avoided and the stability of the process is increased. Furthermore, the frequency may be increased without risk of influencing the following shots. By 3D printing the targets the properties of the block can be controlled accurately. However, preliminary in-house experiments showed severe splashing of the liquid tin when impacted by a high power laser, see figure 1.3.

In both the lithography case and the fusion case the splashing of the surrounding liquid metal is highly undesirable. For fusion a splash will contaminate the plasma and can be the cause of a plasma-killing disruption, for lithography a splash will coat the expensive mirrors and render the machine inoperable. A big difference is the power and timescales of the two phenomena. In fusion a sudden burst of increased heat load on a divertor is called an Edge Localised Mode or ELM. When comparing the typical times and energies of ELMs in JET, ITER, and DEMO with pulse length and energy of the used Nd:YAG laser, a significant difference is noted. Whereas the laser operates in pulses of several nanoseconds and ten micro Joules, the ELMs range in the microseconds and mega Joules. The exact values are summarized in table 1.1. As seen in this table, the peak power of the laser is several orders of magnitude greater than the expected peak power in DEMO. This explains the large splash seen in the previous experiments, the energy transfer during the small pulse length of the laser is immensely fast. Also note that the deposition area of a characteristic ELM is 9 orders of magnitude greater than the deposition area of the laser pulse. And from this point of view, papers stating low or even negligible splashing occurring in tokamaks raise the point of the scalability of this problem. However as stated, the previous experiments done at ARCNL did observe significant splashing, so more experiments are required.

Table 1.1: The pulse time, average power, deposition area, and peak power for a typical ELM expected in JET, ITER, and DEMO and a Nd:YAG laser used in laser ablation of liquid tin and focused to a spotsize of 100µm. ELM values from [12], laser specifications from [13].

	JET ELM	ITER ELM	DEMO ELM	Nd:YAG laser
Pulse time [s]	$1.0 \cdot 10^{-4}$	$1.0 \cdot 10^{-3}$	$1.2 \cdot 10^{-3}$	$8.0 \cdot 10^{-9}$
Pulse power [J]	$4.5 \cdot 10^{3}$	$2.0 \cdot 10^{7}$	$1.0 \cdot 10^{8}$	$1.0 \cdot 10^{-2}$
Deposition area [m^2]	0.43	0.68	5.0	$8.0 \cdot 10^{-9}$
Peak energy [J/m^2]	$1.4 \cdot 10^{3}$	$5.0 \cdot 10^{5}$	$2.0 \cdot 10^{7}$	$1.3 \cdot 10^{5}$
Peak power [W/m^2]	$1.4 \cdot 10^{7}$	$5.0 \cdot 10^{8}$	$1.7 \cdot 10^{10}$	$1.6 \cdot 10^{13}$

As stated, splashing of the liquid metal is an unacceptable phenomenon for both fusion and lithography purposes. Firstly, to suppress or entirely avoid a splash due to laser ablation, the effect of the target surface is investigated. Secondly, the secondary droplets ejected from a splash are analysed to map their commutability from the laser impact case to the droplet impact case. In this project we will be studying the effect of the wetted solid target on the laser ablation splashing and analyse the secondary droplet size distribution for several laser energies. In addition to the desired outcome for ARCNL, a closer collaboration between fusion energy research field and the nano lithography research field is be mutually beneficial.

In earlier experiments conducted at ARCNL, liquid tin splashing by laser ablation is observed. The splashing was observed to crown inward and the volume of tin droplets sprayed around the vacuum vessel was significant (see figure 1.3). To reduce the splashing, while still creating the 13.5nm EUV generating tin plasma, many parameters can be varied. In order to influence the splash several parameters can be chosen to manipulate. The most obvious parameters are: the film thickness, film viscosity, film surface tension, laser pulse energy, laser spot size, laser pulse length, and the target geometry. Since the required liquid composition is pure tin taken at a constant temperature, film viscosity and film surface tension are constant parameters. The first part of this report is focused on variation of the target surface roughness and geometry to influence the splash characteristics. In this report two different research questions were tackled, due to wetting difficulties maintaining an uninterrupted thin liquid layer on top of the target surface. This prompted the decision to use thick liquid layers. However, thick layers exclude the effect of an underlying surface roughness and geometry. Therefore, the second part of the project is focused on analysis of the secondary droplets during laser impact on a thick liquid layer. Due to the different nature of the two parts, this project is split into two different research questions. The original research question:

"Can a substrate geometry for a thin liquid metal film be designed to avoid splashing during laser ablation of a thin liquid tin film for 13.5nm EUV light generation, on a conceptual level?"

And the second research question concerning the droplet analysis on the splashes obtained during laser impact on a thick liquid layer:

"How does fragmentation of the ligaments resulting in secondary droplets during laser ablation splashing to literature on droplet impact splashing compare?"

Firstly, in chapter 2 the theory on droplet impact is investigated for cases of high impact velocity and thin and thick liquid layers. In the case of the thin liquid layers, the focus is on crown evolution, splash velocity, and crown shape. In the case of the thick liquid layers, atomization in secondary droplets, ligament formation, and crown height velocity are of importance. Secondly, in chapter 3 Part I begins with a detailed account of the measurements taken and experiments done is given. This chapter includes the experimental setup during Part I of the project. In addition, a subsection focusing on the production techniques and on the targets is included in this chapter. Next, in chapter 4, the results of the thin liquid layer experiments and geometry investigation are given. This section details observations of the splash on thin liquid layers on varying targets. Also, a novel observation concerning laser impact inside a narrow channel and the effects on the resulting splash are reported. In chapter 5 the results from Part I are discussed. In chapter 6 Part II begins and the experimental setup and processing code is given. In chapter 7 the analysis on atomization in secondary droplets is given. This chapter is based on splashes due to laser ablation of a thick liquid tin film. The results discussed consist of secondary droplet size distributions over time for several energies and their comparison with distributions for droplet impact droplet size from literature. Chapter 8 discusses the results of Part II. Finally, a general conclusion and an outlook of the research is discussed in the last chapters, chapter 9 and chapter 10.

2 Relevant Background

2.1 Splash Dynamics

Characterization of droplet impacts and the subsequent crown evolution has been done for over half a century [14–16]. In droplet impact literature several processes are described during crown formation and evolution. As an incoming liquid droplet hits a liquid film, pressure differences and momentum and energy transfer cause the liquid film to transform, creating (among other things) the so called primary droplets, crown, ligaments, cusps, and secondary droplets. In figure 2.1 these are elucidated with a schematic of a typical droplet impact splash. As the incoming drop makes contact with the liquid film, the drop changes shape due to surface tension forces, viscosity of the liquid, gravity, and its own impact velocity. The extra liquid in the form of the incoming drop will push the liquid film away, creating a pressure difference between the impacted liquid from the droplet and the liquid from the layer which forces the liquid layer to move. Due to inertia and surface tension the extra volume will relocate radially away from the impact location. As stated, the initial drop introduces mass and energy to the liquid film, this extra mass pushes away the liquid film, creating a pressure difference at the interface region. This pressure difference causes the liquid film to deform and create a crown symmetrically around the impact spot as inertia from the surrounding liquid will force the rapidly moving liquid from the incoming drop upward. This crown continues to grow, creating a cylinder shaped sheet of liquid, which eventually could break up at the top edge into smaller cusps and ligaments. These ligaments will, if their growth velocity is large enough, break up into droplets. The produced droplets from the ligaments of the crown are called secondary droplets and are key objects further on in this report. In figure 2.2 the time evolution of the crown after drop impact on a thin liquid film is depicted [15]. In this case the liquid layer is half as deep as the diameter of the incoming drop, indicated by the non-dimensional film thickness δ defined in section 2.2.

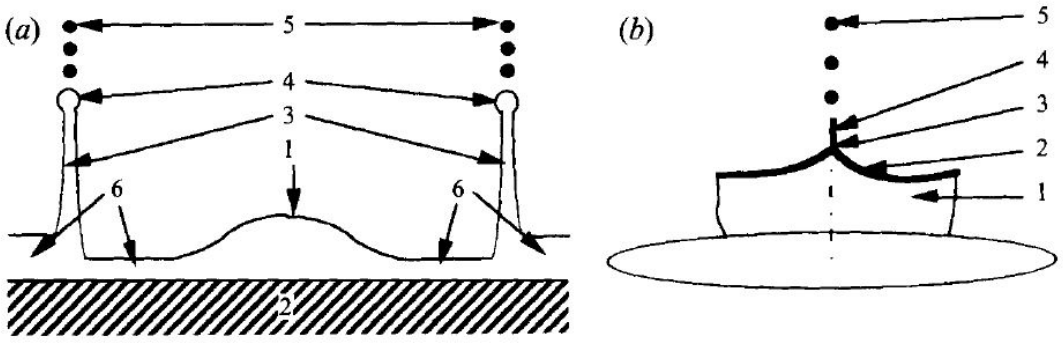

Figure 2.1: (a) A schematic cross section of a single drop impact on a wetted solid surface. 1. residual liquid from drop impact, 2. solid surface, 3. crown, 4. free rim, 5. secondary droplets created from RP instability in ligaments, 6. thin liquid film. (b) section of a free rim after droplet impact with a wetted solid surface. 1. crown like liquid film, 2. top of free rim, 3. cusp, 4. thin ligament created at cusp, 5. secondary droplets. Figure adopted from [17]

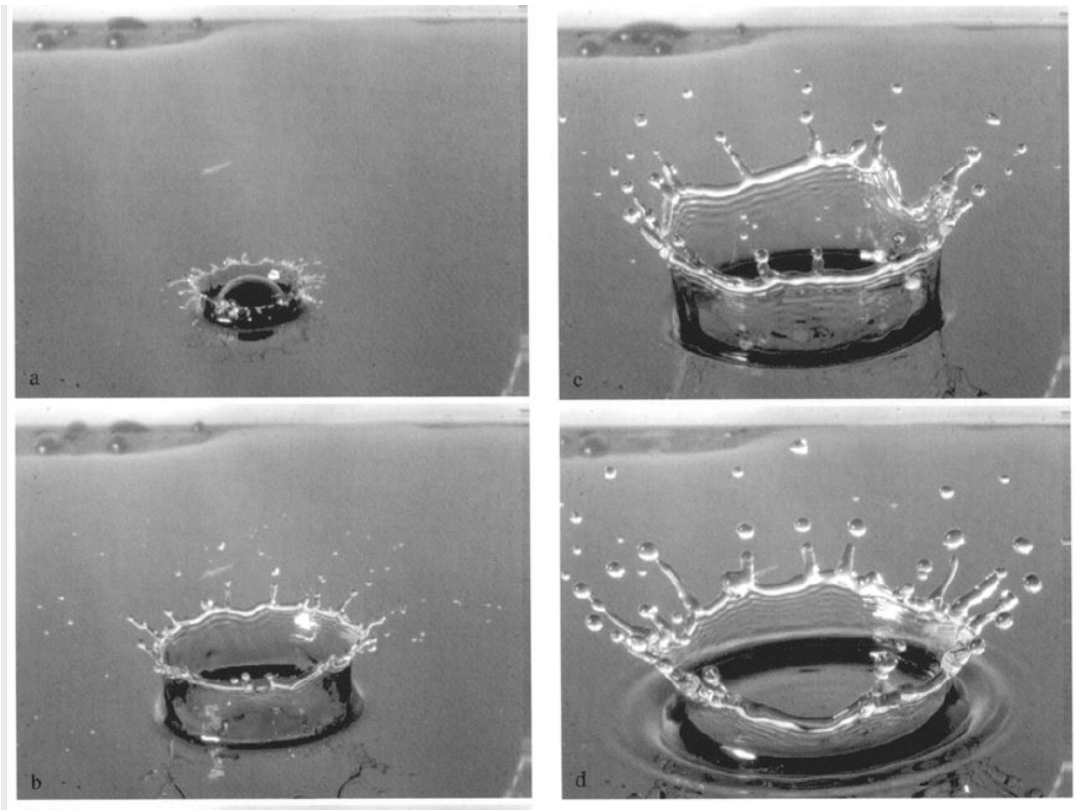

Figure 2.2: Time evolution of a single drop impacting a wetted solid surface. In the figure the crown evolution is shown, including cusp and ligament formation. During the crown evolution prompt splashing is seen as secondary droplets are formed during crown ascend. (a) $t = 0.4$ *ms; (b)* $t = 2.4$ *ms; (c)* $t = 6.4$ *ms; (d)* $t = 12.4$ *ms. adopted from [15].*

In 1995 Yarin and Weiss introduced the concept of the kinematic discontinuity resulting in splashing [17]. This discontinuity in the velocity describes the shock-wave seen at droplet-surface impact, see figure 2.3. The incoming droplet will compress a volume of liquid at the interaction region. This increases the pressure in the impacted volume as the droplet velocity bears on it. The resulting increase in pressure creates supersonic shock-waves in the region. These waves will eventually be released from the liquid volume as the shock-wave velocity is greater than the liquid velocity of the layer after impact. The released shock can create the crown with enough energy to form ligaments. These ligaments will in turn break up into secondary droplets.

Yarin and Weiss also discuss the damping processes for this kinematic discontinuity, stating that the surface tension is the main damping parameter for splashing. In 1997 Cossali et al. thoroughly investigated the impact of a single drop onto a wetted solid surface [15]. They classified the secondary droplet formation into the prompt splash and the delayed splash. Defining the droplet formation from ligaments protruding from the crown during crown evolution as prompt splashing, and delayed splashing as the droplet formation after the maximum crown height. The delayed splash often occurs as the crown film is disintegrating and is broken up into smaller droplets [15]. The dominant parameter in prompt splashing is found to be viscosity [15], whereas in delayed splashing the surface tension becomes the dominant factor [18].

The formation of ligaments on the crown rim is due to the upward velocity and Rayleigh-Taylor instabilities (RTI). The RTI is a growing perturbation due to variation in the densities of the two liquids. This small perturbation can grow to a finger like object, in our case the ligament. The atomisation in droplets from protruding ligaments is due to the Rayleigh-Plateau instability (RPI), an instability dominated by surface tension. In a RPI the liquid column will have a slight perturbation causing a necking of the column. The surface tension forces will cause this perturbation to grown eventually pinching of a section of the liquid column creating secondary droplets

Guo and Wang [19] showed that for low density ratio between the liquid and the gas phase, a bell shape splash is formed.

An example of a bell shape splash can be seen in the top right inset in figure 2.4. This bell shape created as the upper crown is pushed down and inward by drag force of the background gas velocity along on the crown tip. The background gas is pushed away as the crown is formed. The bottom of the crown does not experience the large drag force due to lower background gas velocities at the film boundary. The difference in radial velocity create an inward crowning effect, similar to a bell shape. This background gas velocity responsible for the inward crown, is created by the droplet fall and splash of the initial impact. As the same bell shape is seen in the laser ablation splash, this ratio may have a pronounced effect on the splash.

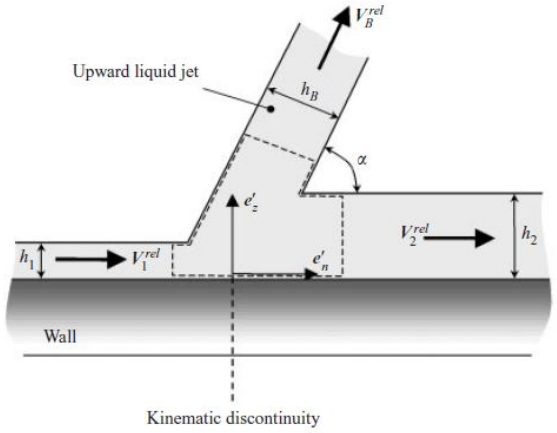

Figure 2.3: The kinematic discontinuity described by Yarin and Weiss. The drop has impacted in the h_1 *region, displacing the liquid film creating a crown with velocity* V_B^{rel} *at an angle* α*. The film thickness outside the impact zone is* h_2*. The interface volume between crown, impact zone, and liquid film is the kinematic discontinuity. adopted from [20].*

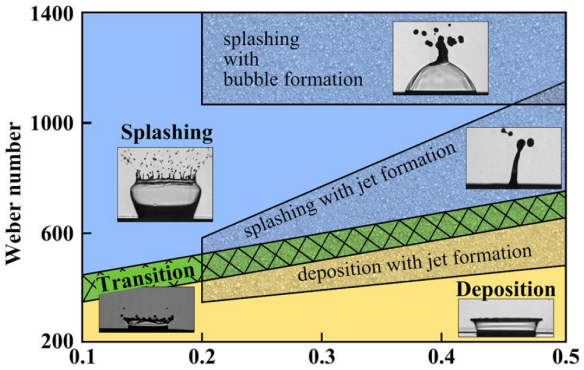

Figure 2.4: A phasediagram for droplet impact on thin liquid films for varying Weber numbers. As seen in the figure, for different layer thicknesses and Weber numbers, the splash has a pronounced different shape at the maximum height. adopted from [21].

One of the defining parameters in droplet impact splashing is the liquid layer thickness. Splash characteristics such as width and height and shape depend on the liquid layer thickness [15, 17, 22, 23]. The distinction for thin and thick layers is based on the non-dimensional layer thickness defined in section 2.2. A thin layer has a thickness in the range of $\delta = 0.1-1$, while we define a thick layer with a thickness of $\delta \geq 5$ [24]. However some papers suggest a thick layer having a dimensionless depth of > 1 [15]. For thin layers the resulting crown from droplet impact is largely formed from the incoming droplet, about 90% of the crown is originating from the mass of the droplet [25]. In the case of a thick liquid layer the resulting crown is approximately 50% compromised of the incoming droplet [25]. This dissimilarity can be explained by the local amount of liquid present in both cases, with a thin layer the local amount available in the layer is much less than the local amount available in a thick layer. As a result the splash shape and time evolution is different for each layer thickness, as seen in the phase diagram in figure 2.4.In this figure the Weber number (defined in section 2.2) is varied as well. A deposition is the formation of a crown which does not eject secondary droplets, a splash on the other hand, is a formation of a crown which does eject secondary droplets. For lower Weber numbers deposition is observed along all measured layer thicknesses, for higher Weber numbers (> 400) splashing is observed for thin layers.

For the drop impact splashing several parameters are found to be of import. These parameters include the surface tension, viscosity, density ratio, and several dimensionless thicknesses. As most dimensionless parameters in droplet impact splash are normalized by the incoming drop diameter, they must be redefined for laser ablation impact.

2.2 Dimensionless Parameters

To effectively describe the processes of liquid drop impact onto a wetted surface dimensionless parameters are used. For droplet impact the film thickness, crown diameter, and crown height are usually normalised by the droplet radius. In this case, where the droplet is substituted with a high energy laser pulse, this normalisation cannot be done by dividing

over the droplet diameter. Instead of using the drop diameter, a characteristic length scale for the laser impact is used to create dimensionless parameters for the film thickness and secondary droplet diameter. In addition to the spatial characteristics of the splash, the time is made dimensionless by normalizing over the characteristic velocity divided by the spot size. These parameters are defined as follows:

$$\delta = \frac{r}{D} \qquad \beta = \frac{d}{D} \qquad \tau = \frac{t}{U/D} \tag{2}$$

With δ as the dimensionless fluid layer thickness, r the absolute fluid layer thickness, D the characteristic length scale for the droplet impact, β the dimensionless secondary droplet size, d the absolute secondary droplet diameter, τ the dimensionless time, t the absolute time after laser impact, and U the characteristic velocity of the fluid. Most of these parameters are well defined in droplet impact literature. The velocity U is defined as the velocity of the incoming droplet and the length D is defined as the diameter of the impacting droplet. To describe the fluid properties the Reynolds, Ohnesorge, and Weber numbers are used, as viscosity, surface tension, and inertia are the most important parameters [16]. The Reynolds number gives the ratio between inertial and viscous forces. A high Reynolds number means inertial forces dominate. The Ohnesorge number gives the ratio viscous to the inertial and surface tension forces. A high Ohnesorge number means viscous forces dominate. The Weber number gives the ratio between the inertial and surface tension forces. A high Weber number means inertial forces dominate. In equation 3 the numbers are given as equations.

$$\mathrm{Re} = \frac{\rho U D}{\mu} \qquad \mathrm{Oh} = \frac{\mu}{\sqrt{\rho \sigma D}} \qquad \mathrm{We} = \frac{\rho U^2 D}{\sigma} \tag{3}$$

With ρ the density of the liquid (and thus $\Delta\rho$ the difference between density of the two phases), D the characteristic length scale of the liquid, μ the dynamic viscosity of the liquid, g the gravitational acceleration, and σ the surface tension. The values for these parameters for liquid tin, which will be used in the experiments conducted in this project, are given with their source in section 2.4.

2.3 Thin Liquid Film Droplet Impact

For the first research question, concerning the effect of the substrate shape and roughness to influence the splash, the thin liquid layer droplet impact case is taken as a benchmark. The layer of the liquid must be in the range of $\delta = 0.1-1$ to be classified as thin [15]. If the liquid layer is too thick, the underlying substrate has little effect on the splash occurring on the interface of liquid to background gas.

2.3.1 The Effect of Substrate Shape and Surface Roughness on the Splash

The geometry and surface roughness of the wetted target has an impact on atomisation of the crown [26]. It is found that increasing surface curvature promotes the onset of secondary droplet generation and crown atomization. Some research is done, e.g. on the splash dynamics on cylindrical surfaces [27]. Increasing positive curvature of the surface can be achieved by shrinking the cylindrical shape, however, below a curvature ratio of 1 (ratio in literature defined as the radius of the incoming droplet divided by the curvature radius of the surface) other processes become important such as rebound, coalescence, and dripping [27]. By reducing the curvature ratio the liquid sheet height of the crown and its corresponding time can be increased [28]. Perturbations of the spreading rim of the film is influenced by the surface roughness [29]. Perturbations decrease in number and increase in size for larger surface roughness.

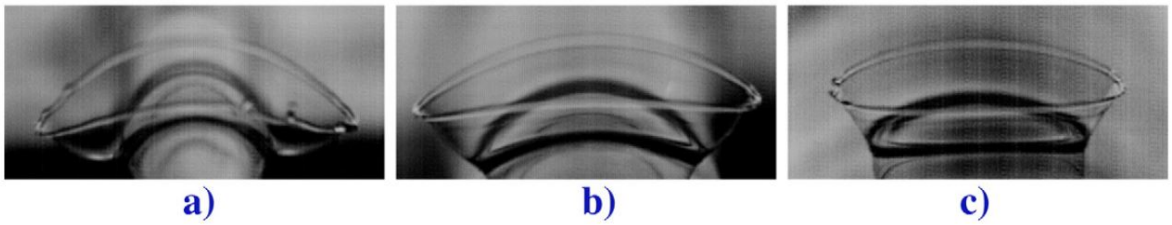

Figure 2.5: Droplet impact on several wetted cylinders with increasing radii. As seen in (a) a cylindrical surface with large curvature and small radius has a significant impact on the crown shape. (b) shows a less curved surface, while still influencing the shape of the resulting crown, and (c) has a small curvature relative to the droplet size thus less influencing the crown shape. Adopted from [28].

By changing the geometry of the target surface, the splash can be influenced. In literature cylindrical and spherical surfaces are investigated using droplet impact. We can conclude that the crown evolution and formation are affected by the different geometries and for increasingly round surfaces relative to the droplet diameter, the crown is growing outward and upward (see figure 2.5) instead of solely upward. Additionally, the dimensionless numbers of Ohnesorge and Reynolds are used to characterize the splash and surrounding fluid as viscosity, surface tension, and inertia are the most important parameters [16]. However, very little of these experiments focus on the splash and formation of droplets.

2.3.2 Wetting of Solids by Liquids

Liquid layer thickness influences the splash and in order to form and control a thin liquid layer, the wetting of the solid surface becomes important. Wetting occurs when the balance between the the surface's free energy and forces on the droplet are such that the droplet spreads out into a layer. Due to surface's free energies that can vary and the small scales of local variation in surface composition, a liquid layer can break up into small droplets sitting on the surface. To measure the wetting of a surface, the contact angle is often used. This is the angle between the surface plane and the liquid surface at the interface point [30, 31]. A high contact angle means liquid drops are formed and bad wetting is observed, a low contact angle means spreading of the liquid. The extreme case of a contact angle approaching 180 °is known as the 'lotus effect' where droplets are sitting as spheres on the surface, whereas the case of a contact angle of 0 °is a smooth layer. In figure 2.6 the contact angle is depicted schematically for bad, intermediate, and good wetting. To improve the contact angle and enable a layer being formed instead of a collection of droplets, the free surface energy needs to be smaller between the solid-liquid interface than the solid-gas interface. A major factor in this, is the formation of an oxide layer on top of the solid substrate. This oxide layer prevents wetting by decreasing the solid-gas interface free surface energy. Another problem is the rapid growth of a thin oxide layer on top of the solid [32]. In addition, a rough surface may improve the wetting capability of a substrate [33]. To speak of wetting of a substrate, the liquid must have a contact angle less than 90 degrees.

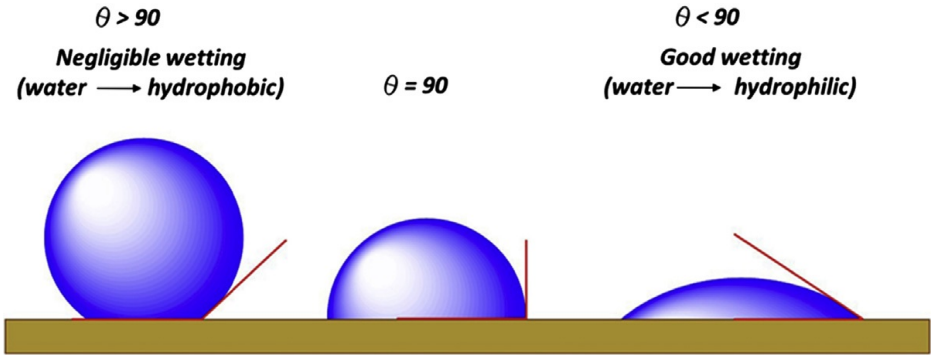

Figure 2.6: Graphical presentation of droplets on a solid substrate, with their respective contact angles. From left to right wetting is increased from bad to good, as seen in a decreasing contact angle. Adopted from [34].

2.3.3 Additive Manufacturing

The samples for this work are produced using Additive Manufacturing (AM) of metal components by means of Selective Laser Melting (SLM). This technique is based on a powder bed method where each layer of material is built from a fine powder. First a fine layer of powder is deposited by a roller or scraper, after which the selected parts of the powder are melted using a focused laser (or melting laser). This will fuse the powder together. To create a second layer the build cylinder is moved down and the roller or scraper deposits a new layer of powder on the sample. Again, the laser will fuse the selected parts together and to the layer underneath. This will build the sample layer by layer from the bottom up. In figure 2.7 the print technique is depicted schematically. When the scanned surface is very rough during SLM production, the next layer of powder will have an irregular depth. This can mean that the laser will not be able to melt a thicker layer of powder thus creating a cavity and increasing porosity. The investigated metal for AM in this project is tungsten.

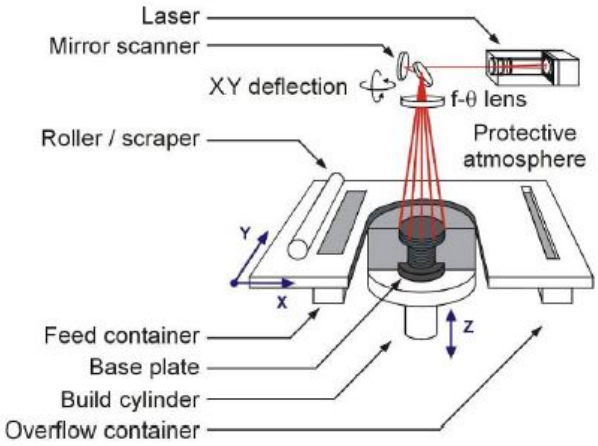

Figure 2.7: Schematic representation of the SLM AM technique. The roller or scraper will deposit a fine layer of material powder on the workspace. The laser will in turn melt the selected parts of this powder sheet to fuse the material together. After fusing the build cylinder will move downward and a new layer of powder will be deposited. Adopted from [35].

The porosity, surface roughness, and microstructure is investigated for tungsten. These parameters may have an effect on the wetting of the targets used and the regeneration of the liquid layer in the project. Almost all products created by additive manufacturing suffer from some form of porosity with respect to traditional casting [35–39]. This porosity is defined as the percentile difference between the global density of a cubic decimeter for an AM manufactured sample and the theoretical density. The theoretical density being the density of a casted sample. The porosity of AM tungsten inherent to the SLM used to manufacture the targets is usually in the range of $2-5\%$. This means the AM tungsten has a density in the range of $95-98\%$ of the theoretical value of $19.25 g/cm^3$ [36]. In figure 2.8 Scanning Electron Microscope (SEM) images of an AM tungsten sample are given. Several micro cracks can be seen as darker lines. The build direction has a significant effect on the orientation of these cracks. For figure 2.8a the build direction is perpendicular to the paper. In figure 2.8b the build direction is vertically upward. In addition, the scanning path of the melting laser also effects the crack orientation.

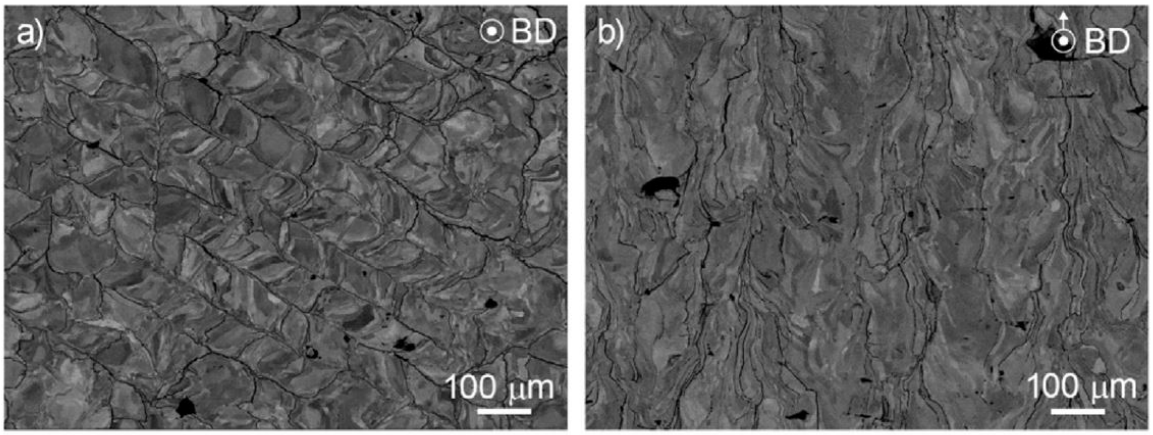

Figure 2.8: Scanning electron microscope images of AM pure tungsten samples. BD in the image shows the build direction of the printing process. The darker lines on the image represent micro cracks and voids in the sample. (a) Top view of the sample, the build direction is perpendicular to the paper. (b) Side view of the sample, the build direction is upward along the surface of the paper. Adopted from [36].

Since the orientation of the sample with respect to the build direction and scan direction is responsible for the orientation of the cracks and pores, it is crucial that the sample is manufactured with the same orientation. As the purpose of the target is to be a basis for the liquid tin film and to regenerate this layer, the supply of liquid tin through the target is an important factor. For regeneration of the layer, the distance between tin supply channels is an important factor as this will determine the uniformity of the tin layer. If the target has a high porosity, more of the tin supply channels are present on the surface, creating a large network of channels filled with tin that can be used to regenerate the liquid layer.

2.4 Liquid Tin Properties

To determine the applicability of the gathered literature about liquid film splashing, the properties of the liquid tin used in the experiments must be investigated. To get a better understanding of the expected splashing characteristics of the laser ablation splash, the surface tension and viscosity of liquid tin for varying temperatures are investigated. To make a prediction of the liquid tin splashing expected in the experiment, the surface tension and viscosity of liquid tin are required to be known. Since the setup at this point does not allow for a detailed viscosity and surface tension measurement system, the temperature dependence on the surface tension and viscosity is investigated. The density of liquid tin is $6.99 \cdot 10^3$ kg/m^3 [40].

2.4.1 Surface Tension of Liquid Tin

Several older papers investigated the surface tension of liquid tin and its dependence on temperature [41–43]. In figure 2.9(a), the dependence of surface tension for pure liquid tin is given as a function of the temperature. In our experiment, the temperature range will be from melting point of pure tin at 231.9 to approximately 300 . As seen in figure 2.9 the data points from Hogness [41], Hoar and Melford [42], and Pelzel [43] fall into this temperature range. However, the values of these experiments do not fully agree with one another. For this project the latest data of Hoar and Melford is taken as the surface tension value. For a temperature of 300 °C this is $550 \cdot 10^{-3}$N/m.

2.4.2 Viscosity of Liquid Tin

In several papers [40, 44, 45] the viscosity of liquid tin is investigated. In figure 2.9(b), the results of Kehr et al. is given as a function of temperature. As stated before, the temperature range interesting for this experiment is from the melting point of tin (231.9 °C) to approximately 300 °C. The viscosity value for a temperature of 300 °C is $1.4 \cdot 10^{-3}$Pa s.

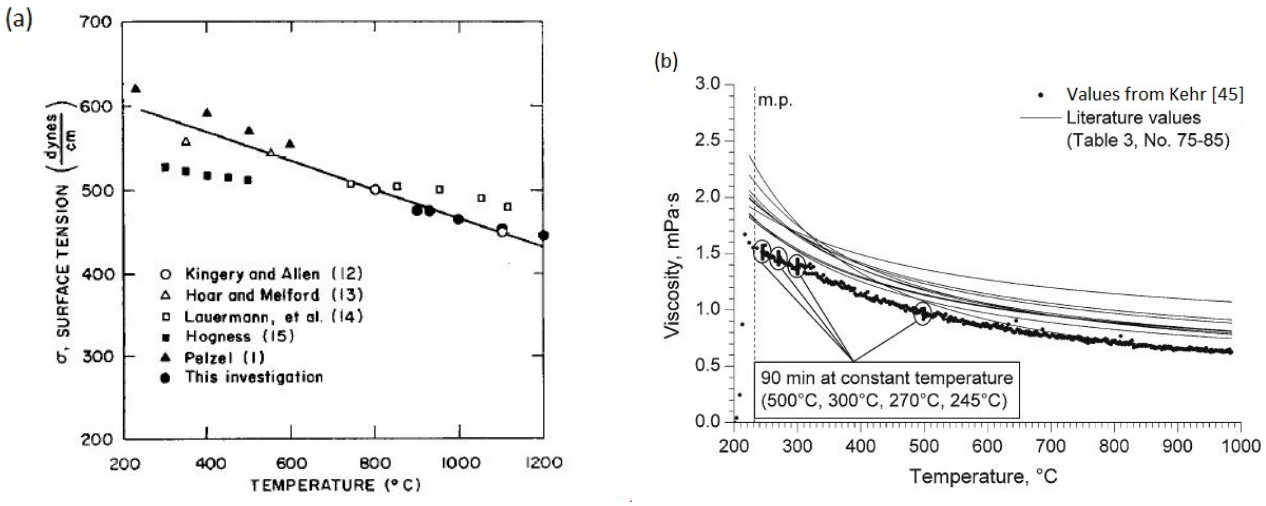

Figure 2.9: (a) Surface tension of pure liquid tin as a function of temperature. The surface tension is given in dynes/cm, this is equal to mN/m. Adopted from [46]. (b) The viscosity of pure liquid tin and its dependence on temperature. Adopted from [44], with literature values from [45]

2.5 Secondary Droplet Formation

The second research question, focuses on the atomization in secondary droplets and evolution of the corresponding ligaments. Thick liquid layers are layers with $\delta \geq 1$ according to Cossali [15], or according to Engel layers with $\delta \geq 5$ [24]. Since it does not matter if the layer will become thicker, we will adhere to Engel's definition of a thick layer.

Droplet size distributions found in literature are typically done for thin liquid layers, since thinner layers increase the amount of secondary droplets created [18]. Seen in figure 2.10, the droplet impact on the very thin layer ($\delta = 0.05$) is starting to eject secondary droplets at 3ms and the entire crown sheet breaks up at 6 ms. The thicker layer ($\delta = 0.5$) starts to eject secondary droplets at 3 ms as well, but does not show crown sheet break up even at 10 ms. In both cases the liquid composition, droplet velocity, temperature, and background pressure and composition are equal [22]. Since droplet formation literature on thin liquid layers is much more common, most information from this literature is taken. We focus on the information concerning Weber number dependence, radius of droplets, and droplet size for droplets that are originating from ligaments on the crown rim, not from crown sheet breakup. For this purpose figure 2.11 displays droplet size distributions for several different Weber numbers. On the vertical axis the counts are given from the phase Doppler anemometer in the experiments used by Mundo et al. [47], which shows the amount of droplets detected. On the horizontal axis is the normalized droplet diameter, normalized by the original impact droplet diameter. For lower Weber numbers the distribution is wider than for larger Weber numbers, where the distribution is narrower. Often in droplet impact literature, Weber number is varied by variation of the incoming droplet velocity. In addition, the whole distribution shifts toward smaller droplet diameter for higher Weber numbers. A higher Weber number means smaller droplets as seen in figure 2.11. For calculation of the splashing parameter, U and D must be known. To determine the impact velocity in droplet impact, the terminal velocity of the impacting droplet is usually taken. However, with laser ablation splashing, no incoming droplet is present, only the laser beam. To determine the impact velocity U for the laser impact case, the work of Kurilovich et al. is taken as input for this parameter [48]. In the experiments by Kurilovich, a 30 µm diameter droplet is impacted by a Gaussian laser pulse midflight. This impact transfers momentum to the droplet. The gained velocity of the droplet by the laser impact is measured and shows a dependency on the laser energy following the power law [48, 49] given below in equation 4.

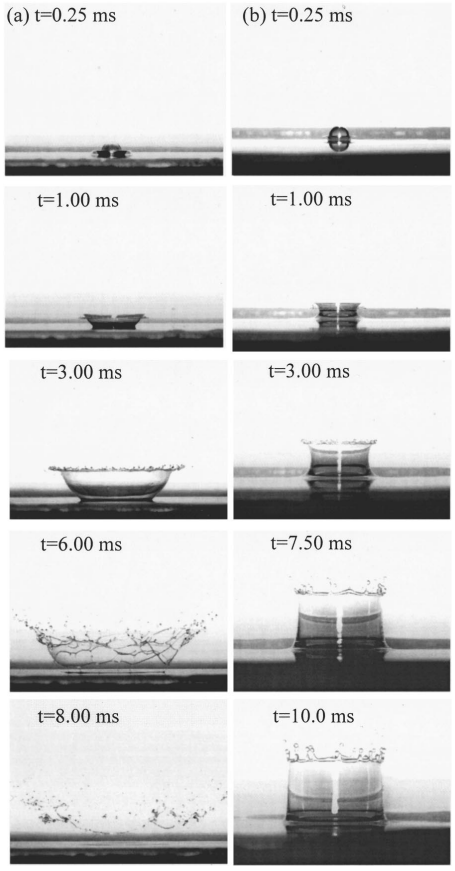

Figure 2.10: Two droplet impacts, both with We = 2107. The liquid used is a 70% glycerol-water solution. (a) The layer has $\delta = 0.05$, the crown starts to eject and form secondary droplets around 3 ms. After 6 ms the sheet of the crown is breaking up into smaller droplets. (b) The layer has $\delta = 0.5$, the crown in this case starts to from secondary droplets at 6 ms. In this deeper layer case, the crown remains intact throughout 10 ms after droplet impact, in contrast to the thinner layer case. Adopted from [22].

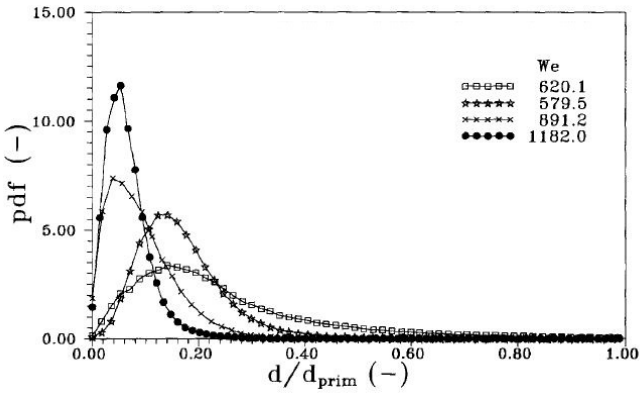

Figure 2.11: Droplet distributions for several Weber numbers. The horizontal axis shows the secondary droplet diameter normalized by the incoming (primary) droplet diameter. On the vertical axis the amount of counted droplets is given. Adopted from [47].

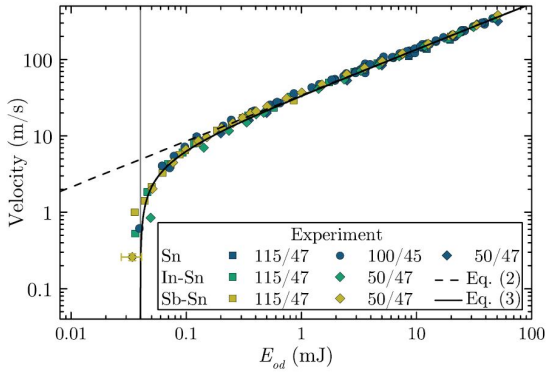

Figure 2.12: The power law of Kurilovich derived from experimental data. On the horizontal axis is a log scale of the energy of the laser pulse. The vertical axis shows a log scale of the resulting velocity of the impacted droplet. The power law begins as a parametric function and reforms to a linear one after 0.2*mJ. Adopted from [48].*

$$U = K_u E_{od}^{\alpha} \tag{4}$$

with U the droplet velocity, K_u a proportionality constant, E_{od} the energy on the droplet, and α an exponential factor found to be 0.6 for $E_{od} \geq 0.2$mJ [48]. In figure 2.12 the power law is given graphically.

In addition to the work of Mundo [47] on droplet distributions and Weber number, Villermaux tackles distribution fits. For secondary droplet formation from ligaments Villermaux states a Gaussian distribution to fit best for the droplet size. For crown sheet breakup and atomization into secondary droplets, as well as atomization of droplets into secondary droplets, Villermaux states a Gamma distribution to fit best [50, 51]. A Gauss distribution is given in equation 5.

$$P = \frac{A}{w \cdot \sqrt{pi/2}} \cdot \exp(-2 \cdot \left(\frac{x - x_c}{w}\right)^2) \tag{5}$$

In which P is the probability, A the area under the curve, w the width of the curve, x_c, the most probable value, and x will be Villermaux's input value. Additionally, a dependency of the mean rim diameter by the Weber number is observed by Villermaux, following the equation:

$$\langle d_{sd} \rangle \propto h \cdot We^{-1/4} \tag{6}$$

With $\langle d_{sd} \rangle$ the mean rim diameter at a certain time after impact (not to be confused with crown diameter), h the sheet thickness, and We the Weber number. From equation 6 follows that for higher Weber number and lower sheet thickness, the mean rim diameter decreases. The Weber number for the laser impact can be described with the help of equations 3 and 4.

2.6 Laser Ablation Splashing

High initial pressure difference between the liquid film and the plasma cloud will decrease the importance of surface tension and viscosity of the liquid in favor of inertial forces [20]. The inertial effects will dominate the splashing behavior, and the crown evolution as described by a moving rim is dominated by the surface tension.

At ARCNL a preliminary experiment is conducted to explore the splashing caused by YAG-laser ablation of a thin liquid tin film over a tungsten target with microstructure and capillary pores. In figure 2.13 the time evolution of the laser ablation splash is given. This splashing occurs during a period of $2 \cdot 10^{-4}$s, while laser ablation of a liquid is a process in the 10^{-10}s time scale. So the ablation can be approximated as instantaneous. Note that the time- and length scales between figure 2.2 and figure 2.13 differ by 3 orders of magnitude. The plasma expansion due to the ablation of the

liquid will create a high pressure in the interface area, similar to the pressure created by a drop of liquid impinging on a liquid film. To elucidate the splash, the pressure propagation of the resulting plasma by laser impact is investigated.

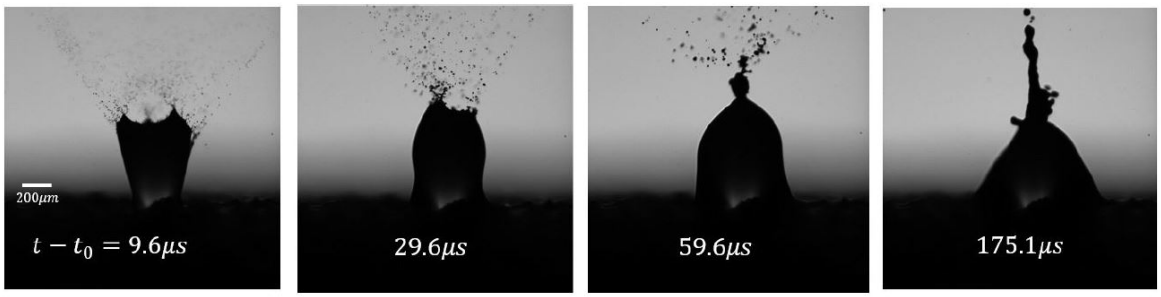

Figure 2.13: The splash caused by laser ablation of the thin tin film over a tungsten target for different times after laser impact. Figures produced using shadowgraphy. Scale is given in the leftmost figure. The layer thickness of the tin is unknown, laser energy is 10 *mJ for a duration of* 0.5 *ns for a focused beam. As seen the secondary droplet formation throughout the splash is significant. Courtesy of B.Liu from ARCNL.*

2.6.1 Ablation Pressure Propagation

The laser will not add extra liquid to the film, but instead rapidly ablates the strike zone. As the liquid ablates into a plasma, a pressure difference is built along the interface of liquid and gas/plasma due to the plasma expansion. This pressure difference triggers the formation of a crown similar to the pressure difference imposed by the drop impact would as seen in figure 2.13. As the laser impacts the liquid film, in the time of a nanosecond the first part of the laser pulse is absorbed in the liquid film causing it to ablate. The larger part of the pulse is then absorbed into this vapour cloud created by the ablation of the liquid, creating a hot, expanding plasma. This plasma expansion outward from the laser spot is responsible for the pressure difference that causes the liquid to form a crown. Gonzalo et al. define a plasma length as the maximum distance a plasma expands. This plasma length is reached after the gas and plasma pressures equilibrate using an adiabatic model [52]. The equation for the plasma length as defined by Gonzalo et al. is given in equation 7.

$$L_p = A[(\gamma - 1)E]^{1/3} P_0^{-1/3\gamma} V_i^{(\gamma-1)/3\gamma} \quad \text{with} \quad V_i \approx v_0 \cdot t_{pulse} \tag{7}$$

With L_p the plasma length, A a geometric factor related to the laser spot shape, γ the specific heat ratio, E the laser fluence, P_0 the background gas pressure, V_i the initial volume of the plasma, v_0 the initial velocity of the plasma species, and t_{pulse} the pulse length of the laser [52]. The plasma length for tin plasmas created in the preliminary experiments is on the one meter scale.

Part I

Target Geometry Investigation

3 Experimental Method

3.1 Experimental Setup

Here the experimental setup used in the experiments is described. In figure 3.1 the setup is depicted in a diagram. The high power laser used in this project is a SureLite S I-10 (YAG type laser) operating with the parameters provided in table 3.1. The outgoing laser pulse will pass trough a Thin Film Polarizer (TFP) where some of its power is redirected to a beam dump, reducing the energy of the pulse. After the TFP the beam passes trough a polarizer and another TFP at a right angle of the first TFP. This allows for control of the energy of the resulting laser pulse through variation of the polarizers orientation. After this the beam passes a beam expander consisting of 2 lenses, one concave (f = -150 mm), one convex (f = 300 mm), chosen to increase the area of the beam with a factor 2. After this, the laser beam will pass through a focusing lens, which will focus the beam into a spot on the target. By varying the position of the focusing lens the size of the spot on the target can be changed. The location of the laser spot is changed with a tens of microns precision by tilting the final mirror in the beam path. The final mirror is mounted in a Thorlabs Rear-Loaded, Clear-Quadrant Kinematic Mirror Mount (KM05FR). The target is held in place by the targetholder. This is a block of gold coated copper, fitted with a heat element and a thermocouple to heat up and measure temperature respectively. The imaging of the resulting splash from laser impact is done using the shadowgraphy laser. This laser also passes 2 TFP plates and a polarizer to reduce its energy. Then it is focused using a focusing lens and is absorbed by a dye cell. This dye cell will in turn emit light with wavelength of $\lambda = 532$ nm and an intensity dependent on the incoming laser energy. Using an optical fiber, the light from the dye cell is transported to a mirror array near the vessel, which will create a parallel beam of light shearing the surface of the target and providing a back light for the CCD camera. This camera is then triggered once a splash occurs to capture the shadow of the splash. Since the CCD camera needs time to capture a splash, every image is taken from a new splash.

Table 3.1: Laser parameters of the main laser pulse used in laser ablation of the liquid tin film.

Laser parameter	**Value**
wavelength	1064 nm
pulse length	8 ns
frequency	10 Hz
energy	5 - 20 mJ

The resulting main laser beam profile after the focusing lens is measured using a CCD camera. To measure the profile the main beam is temporary redirected to focus on the CCD. This allows us to measure the diameter of the FWHM of the Gaussian laser beam. This value will be used to indicate the spot size of the laser. In figure 3.2 the beam profile is given for Part I. The green ellipse is the measured beam at the FWHM, the lines indicate the orientation of the major and minor axis. The spot size is 50 μm in diameter, with a slight variation in the outer region of the spot, making the resulting spot slightly elliptical. This effect can be better seen in figure 3.3. Here the curves of relative intensity along the major and minor axis are given. In the relative intensity profile at the edge a slight increase can be seen inside the red circle, influencing the splash resulting from this laser beam. The splash seen is slightly asymmetric due to the asymmetry in the laser profile.

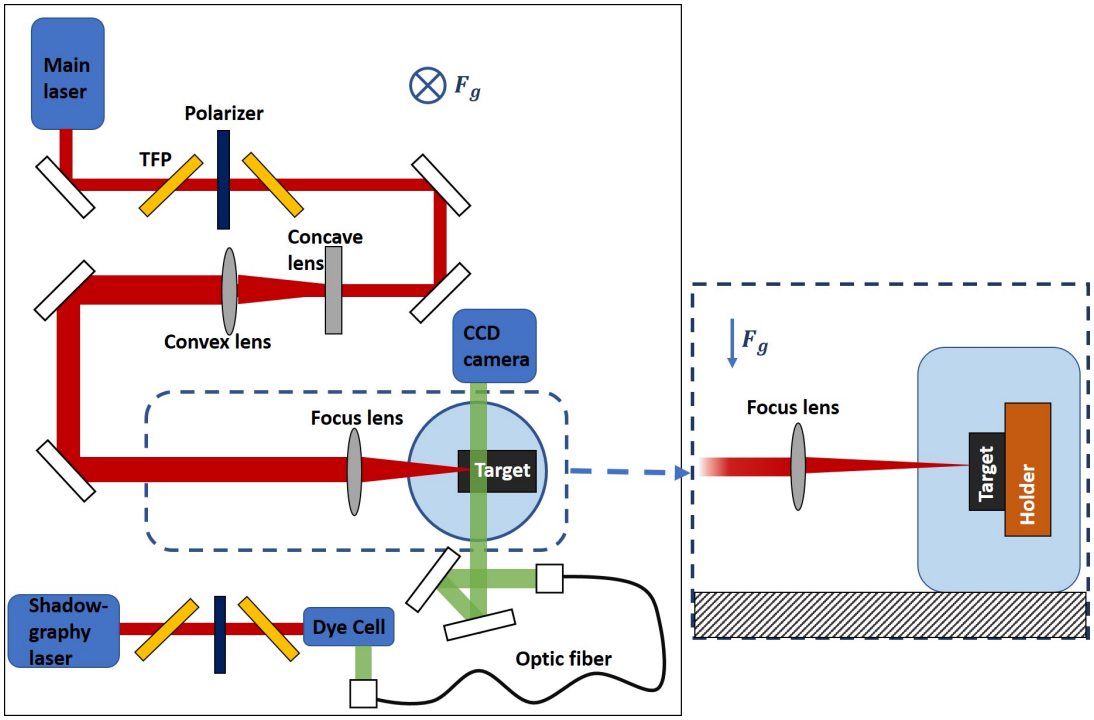

Figure 3.1: A schematic representation of the experiment including the shadowgraphy setup, target, and YAG laser from a top view. The laser beam path is given as a red line beginning at the main laser and terminating at the target. The blue circle is the vessel, which is kept at a medium vacuum. The green line represents the light from the dye cell used as back light for the CCD camera. The cut-out on the right shows the last leg of the laser path from a different angle. The cut-out section shows the side view of the focus lens, vessel, target, and targetholder.

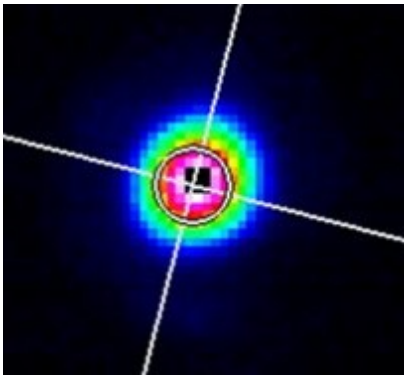

Figure 3.2: The 2D beam profile as measured by the CCD camera after the focusing lens for Part I. The profile is at the focus point of the lens. The white cross represents the major and minor axis of the measured spot. The measured spot is given as a green ellipse.

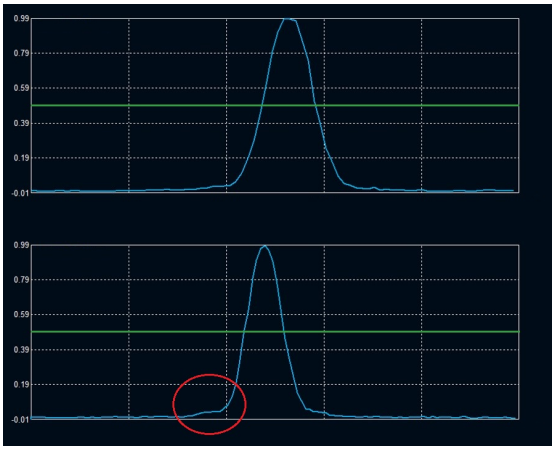

Figure 3.3: The relative intensity curves along the major and minor axis from top to bottom for the laser beam used in Part I. The vertical axis shows relative intensity, the horizontal axis the position along the major and minor axis in µm. Both curves show a Gaussian, the bottom curve has a small shoulder on its left pointed out by the red circle around it. The green lines show the FWHM.

3.2 Experimentation Process

Experimentation is done at ARCNL in Amsterdam, where the experimental setup was built from scratch. The imaging of the splash resulting from main laser impact on a liquid tin layer is done using shadowgraphy. This shadowgraphy uses a separate laser to supply back light for the CCD camera. During the experimental campaign several different targets will be shot with the high powered YAG laser. The location of the main laser can be visible by eye, due to the resulting plasma light of the ablation, allowing for millimeter precise localization of the laser spot. The laser is translated over the surface by tilting the last mirror in the beam path. In addition, after experimentation the laser path was often visible on the target (see discussion in section 5). In addition, the temperature of the target, gas pressure in the vessel and the film thickness are kept constant for each shot. The temperature is controlled using a heat element and thermocouple coupled to a controller, keeping the temperature constant on 300 °C. The background pressure is constant after 1 hour of pumping by the vacuum pump used in the setup, being for all experiments in the range of $0.05-0.10$ mbar. The values for temperature and background pressure apply to all further results unless explicitly stated otherwise. The images of the resulting crown formation by laser impact are captured using a specialized software created by AMOLF, which controls a delay generator to time the delay between main laser impact and shadowgraphy laser. This delay allows the camera to capture an image with nanosecond accuracy in time. By changing the delay, different stages of the splash are captured and stored by the software.

3.3 Target Production

The targets are produced using SLM. In section 2.3.3 an account of this manufacturing technique is given. In the end, the choice of target material was chosen to be tungsten. This decision was due to the large porosity, high melting temperature, and chemical compatibility with tin. In addition, the expertise of printing fine structures accurate to several tens of micro meters of the producer (Royal Philips Dunlee) was desirable.

3.3.1 Target Designs

To investigate the effect of the substrate surface roughness and geometry on the thin layer laser impact splash, several designs were created. These were based on a standard design for the target holder in the setup described in section 3.1. A cross section of a tree target as designed by Rindt [53] is shown in figure 3.4a. A cross section and schematic of a flat table target is shown in figure 3.4b and 3.4c respectively. In figure 3.4b the reservoir which holds the liquid tin is shown. In figure 3.4c a reference pillar, moat and table are pointed out. The reference pillar was used to calibrate the pixel size of the images. The moat is added to prevent wetting of the reference pillar and the table is the laser receiving surface of the target.

The tree target seen in figure 3.4a has a surface texture pattern consisting of small, hairlike pillars. These pillars are enlarged in the SEM cut-out of figure 3.4a. Below the surface several capillary channels rise from a reservoir to the surface, while decreasing in channel width. These channels allow a capillary flow of liquid tin from the reservoir to the surface and have a diameter at the surface of 10 μm. They are distributed in a square pattern 2 mm in size on the surface. These targets are produced by means of AM of the type SLM.

The flat table target seen in figures 3.4b and 3.4c has been designed in cooperation with J.C.J. Hermens. The flat table surfaces are 3×3 mm, with a 0.1 mm capillary channel surrounding them. This channel allows liquid tin to flow from the reservoir underneath the surface to the surface. The reservoir is in direct contact to the back side of the target through eight cylindrical channels to allow new tin to flow in the reservoir. These targets are produced by means of AM of the type SLM.

3.3.2 EDM

EDM also known as Electrical Discharge Machining, is a high precision production technique often used to cut materials that are hard to machine using traditional drills and saws. To create a smooth surface, the discharge was swept along the surface of the target. EDM uses a wire to guide the discharge, the diameter of the wire imposes a minimum radius and roughness obtainable. Used for the targets, was a wire with a diameter of 20 μm. The theoretical surface roughness of the flat table target was manufactured to be an average roughness of 20 μm. However, due to the printed nature of the samples, small pores are present in the targets. These pores locally increase the surface roughness by a value between the minimum and maximum expected pore size in tungsten.

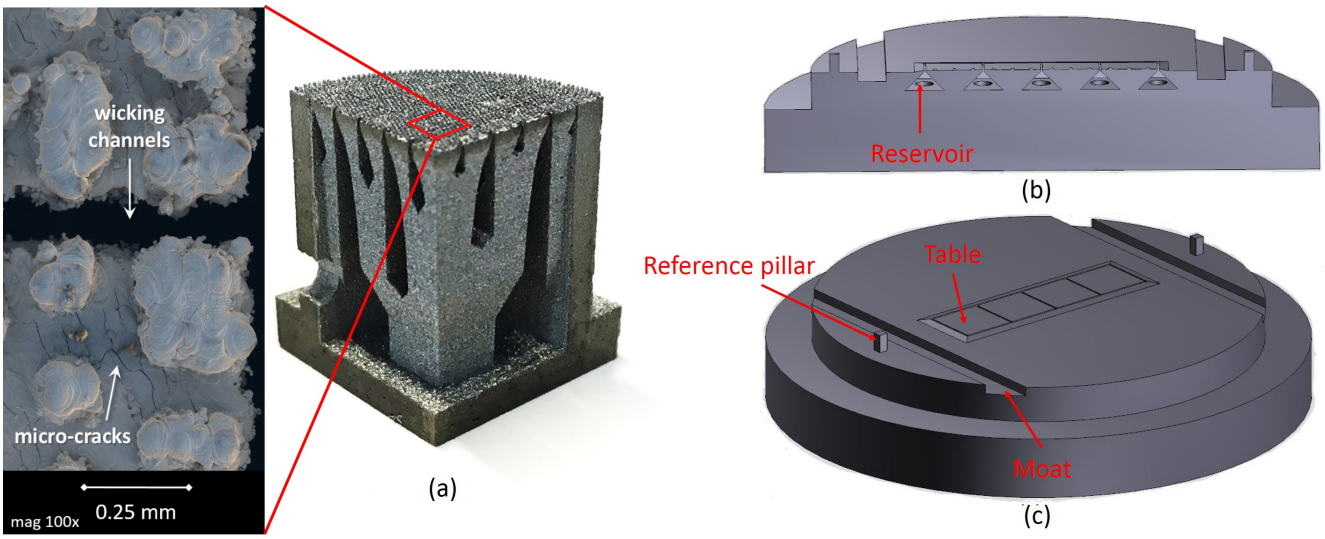

Figure 3.4: (a): A cross section of the tree target with capillary channels to the surface. On the surface a surface micro pattern is present as seen in the cut-out. The cut-out is a SEM image of the top surface, with wicking/wetting channels, micro-cracks, and the pillars. The total height is 17mm and diameter of the top is 25mm. Adapted from [53]. (b): A cross section of the flat table target design with flat tables and capillary channels. The tables are 3 × 3mm and the capillary channels are 0.1mm at the surface. (c): Overview of the flat table target with capillary channels. At the top and bottom of the target is a moat and a reference pillar.

3.3.3 Wetting of Targets

Originally the targets were wetted with tin in a vacuum of $1*10^{-6}$ mbar by heating the target to high temperatures via an inductance ring. No temperature sensor was present in this setup and exact temperatures of the target reached during the wetting process are unavailable. Estimated maximum temperature of the tungsten sample was 2000 K, as the sample was glowing. Wetting in this setup was achieved by placing an amount of tin on the top of the target and inserting it within the inductance ring. After reaching the required pressure the temperature was increased by switching on the current in the ring. This was done at DIFFER. Visually, the target will become glowing hot (bright red color) and the tin will melt onto the target. It is speculated that high temperature and low pressure are needed to eliminate and prevent regeneration of the oxide layer between the tungsten and tin surfaces. Another wetting method was performed at ASML in a radical hydrogen environment, resulting in thinner uninterrupted layer on the surface and less contamination in the tin. After this wetting treatment extra tin was supplied to the target through the hole seen in the lefthand side of the tree target in figure 3.4a, or in the case for the flat table target designs, from the back of the target.

3.4 Targets Used in Experimentation

Two different target designs and a total of three different targets are used in the experimentation for Part I. To distinguish each target they are numbered.

3.4.1 Target 1

Target 1 is a tree target. The target was previously used and filled with tin, the top most 100 µm of tin was removed by means of EDM to clean the target. Target 1 was wetted with 99% pure tin in the vacuum induction oven at DIFFER. The top surface was shiny gray after wetting, however, the underlying pattern of pillars was still visible. In figure 3.6 target 1 is shown before experimentation. Target 1 has several regions that have a slightly different color of gray with respect to the rest of the surface. This color change may indicate a slight contamination of the tin on the surface.

3.4.2 Target 2

Target 2 is a tree target. The target was rewetted in a high vacuum radical hydrogen environment resulting in a thin tin layer. The top surface of the target after wetting was dull gray and covered with a layer of pure tin. The tin was sufficiently thin to see the underlying pattern of pillars by eye. In figure 3.7 target 2 is shown before experimentation. The color of target 2 is noticeably different from the color of target 1. This color difference may be attributed to the different wetting conditions for each target, however, the exact reason is not known.

Figure 3.5: Target 3: Flat table target, wetted at DIFFER.

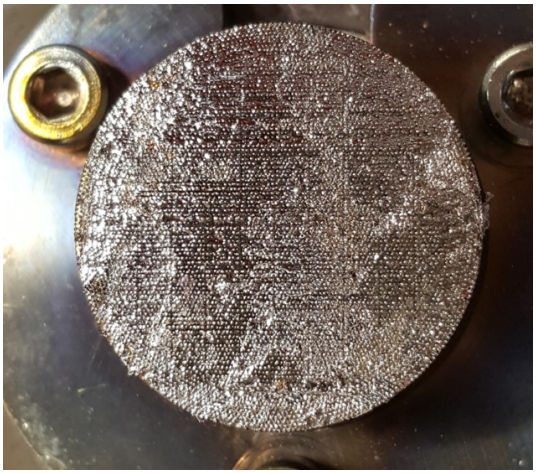

Figure 3.6: Target 1: Tree target, top 100 µm EDM'ed off, wetted at DIFFER.

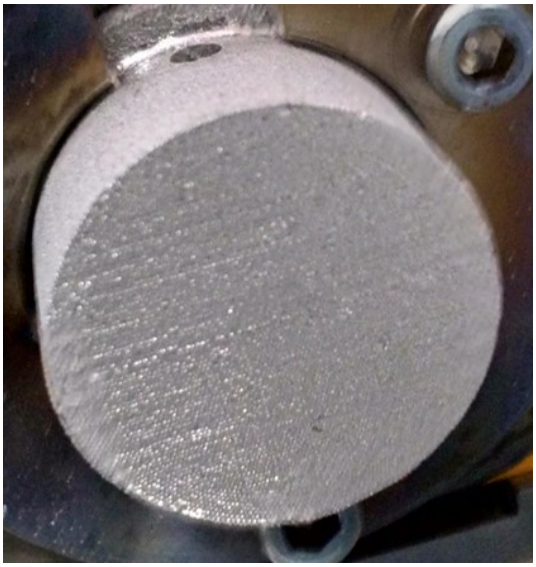

Figure 3.7: Target 2: Tree target, wetted at ASML in radical hydrogen environment.

3.4.3 Target 3

Target 3 is a flat table target. The target was manufactured by Philips Dunlee and the surface roughness was reduced using EDM at the EPC. Wetting was done in the vacuum induction oven using a ceramic ring to hold the tin in place while melting it on the target. The tin did not creep into the reservoir and cylindrical holes at the bottom of the target after wetting. On target 3 the tables and channels around them are still visible indicating a thin layer of tin on the surface. The gold discoloration is probably due to heating and cooling of the target both done in medium vacuum of the experimental setup and in atmosphere during refilling of the liquid layer.

4 Results

Although systematic variation of the targets was intended, due to wetting issues this was not possible. Nevertheless, preliminary results illuminate the influence of geometry. In this section the preliminary results of the laser ablation splash for Part I are given. The targets used are described in section 3.4.

4.1 Results of Target 1

The first results were obtained using target 1, with a laser energy of 10 mJ and spot size of 50 µm. This target is inserted into the targetholder such that the orientation of the rows of pillars are orthogonal to the worktable. This allows for precise translation of the laser up and down along a row of pillars. This translation along the pillars can be seen in figure 4.1. In this figure the laser is translated from top to bottom in the images (a) - (i). The total translated distance of the laser is 310 ±20 µm from image (a) to image (i). Starting at figure 4.1(a) the laser creates a chaotic splash, with a crown that is breaking up immediately. In b) this breakup is continued, as is the case in (c). In (d) only a ligament above the laser spot can be seen. In (e) no crown is visible above the surface of the target, this is suspected due to the absence of tin on top of the pillars. In images (f) to (i) the crown slowly starts to form again, first at the bottom side of the plasma spot, then all around the spot. In (i) the crown resembles the chaotic crown of (a) upside down. The pillar locations depicted in the cartoon images of figure 4.1 are suspected locations.

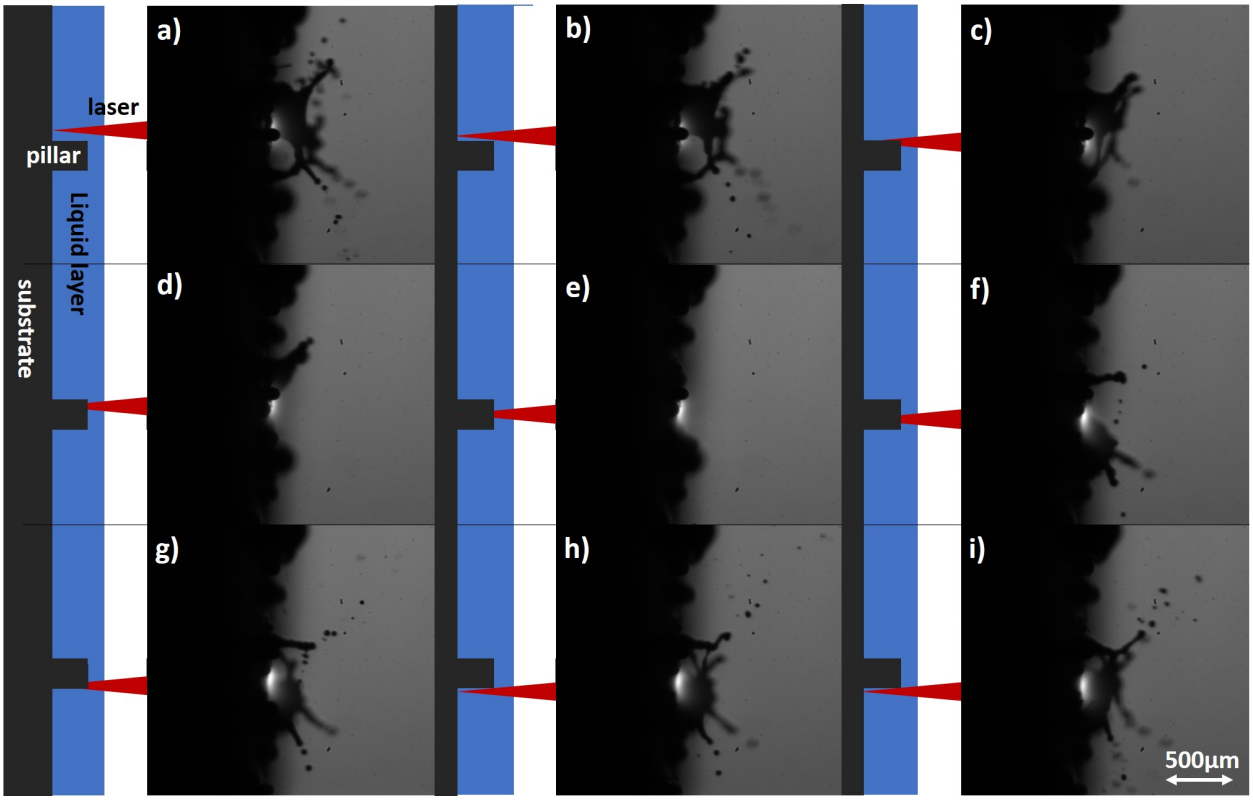

Figure 4.1: The resulting crowns after laser ablation while the laser is translated a total of 310 ±20µm over the surface of the target downward. The laser energy is 10 mJ and the spotsize is 50 µm. In all images the location of the impacting laser is highlighted by the emitting plasma. In (a) a crown is visible. In the 3 following images (b-d) the crown's downside vanishes as the laser spot is translated down. In (e) no crown is visible. After this (f-h), the crown starts to form again, starting at the lower side and projecting ligaments in a downward preferred direction. In (i) a crown can be seen. Next to each sub-figure a cartoon of the laser, pillar, substrate, and the liquid layer is given as an indication of the relative laser spot and pillar location. The pillar and substrate are depicted in gray, the laser in red, and the liquid tin in blue.

4.2 Results of Target 2

The second set of experiments were performed with target 2 with laser energy 10 mJ and spot size 50 µm. In figure 4.2 a splash is given over a span of approximately 3600 laser impacts. The delay of the camera after laser impact is kept constant. This figure shows the effect of repeated laser impact on the same location over real time. The splash seen in 4.2(a) is the benchmark for a normal splash in this case. After 290 impacts, the crown starts to significantly change shape. A break up of the crown sheet is seen and continued in (c) and (d) at 770 impacts and 2650 impacts respectively. After 3160 impacts in (e) the crown is almost completely gone, with the exception of a small triangular liquid shape at the base of the lower ligament. After 3680 impacts, this last lower ligament has decreased in length as well. In (f) a large circular tin droplet is seen at the bottom of the crown. Regrettably, no information about substrate damage is recorded after experimentation. As this experiment is done on targets with the tree design, which have a larger fraction of supply channels for tin, it is suspected that the flat table targets are have a lower regeneration rate of the liquid tin layer.

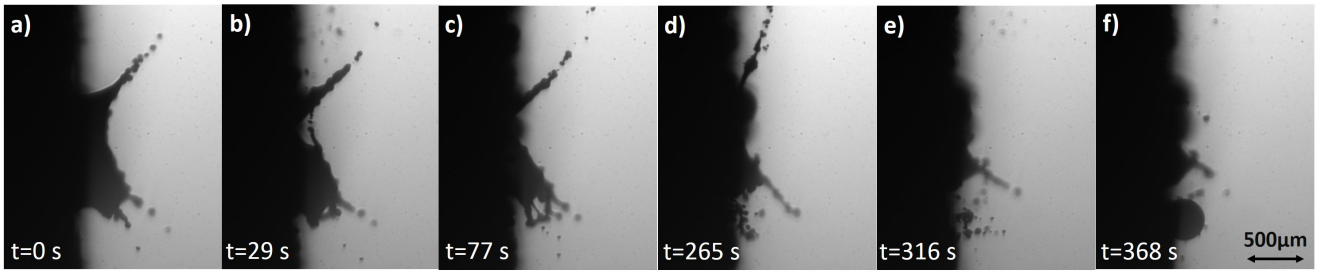

Figure 4.2: A crown resulting from laser ablation over a period of 6 minutes for the first and last image. The laser energy is 10 mJ and the spotsize is 50 µm. Over time, the crown breaks up into large ligaments instead of a liquid sheet. In the end, a small ligament with a very small sheet can be seen.

Furthermore, during the second set of experiments a droplet was seen to be hanging on the lower side of the target after repeated laser impact. This droplet, consisting of tin, has a varying layer thickness at the edge of the droplet. The images in figure 4.3 the upper edge of the hanging droplet is seen. This droplet edge is targeted with the main laser and the resulting splash is captured. The blue cross present in the figure gives the impact location of the laser. The red line in the approximate location of the substrate. The laser energy was 30 mJ with a spotsize of 66 µm. In figure 4.3 the laser location is translated upward from (a) to (c), this translation upward over the sloped surface of the droplet results in a decreasing layer thickness at the laser location. The layer thickness is approximated by the distance of the laser spot to the substrate (which is presented by the red line). In (a) this approximate thickness is 270 ±50 µm, for (b) is 210 ±50 µm, and for (c) is 160 ±50 µm. The uncertainty is approximated, keeping in mind the exact laser spot is suspected at the middle of the splash and the substrate surface is suspected to be at the red line. In figure 4.3(a) a crown can be seen with ligament and secondary droplet atomization. The crown is tilted slightly to the left as seen from the normal of the liquid surface. In (b) the laser spot moves up to the edge of the droplet. The crown is breaking up on the left side, where the layer thickness is less than on the right side of this crown. In (c) the laser spot is moved up even further resulting in a spray of droplets, one large stream of droplets at the bottom, and no visible crown. From (a) to (c) the laser spot is translated upward approximately 500 ±100 µm along the surface of the liquid layer. Again, the target was not checked for damage on the substrate after experimentation.

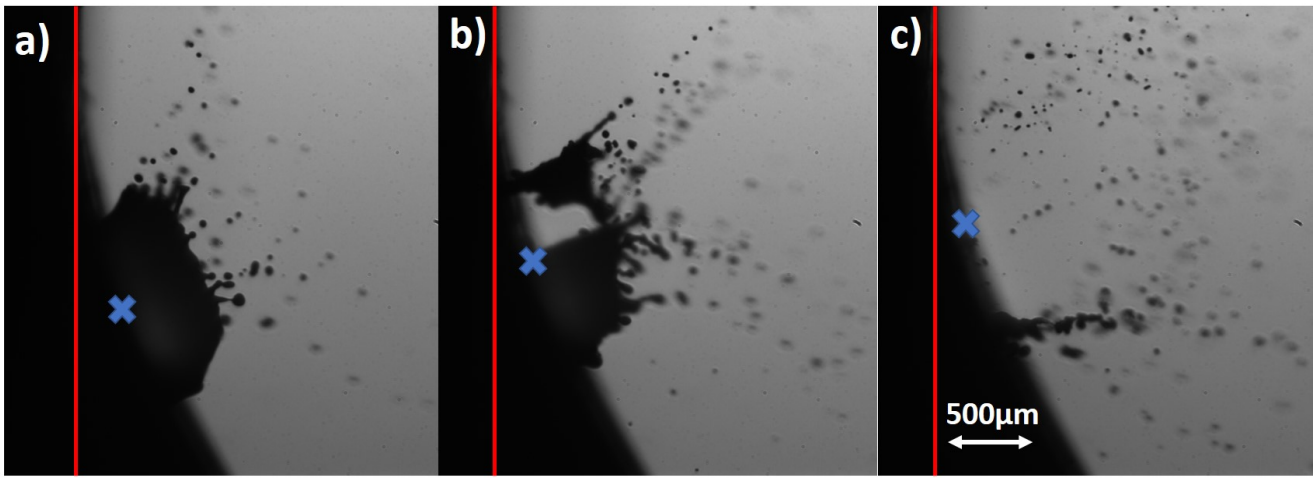

Figure 4.3: A crown resulting from laser ablation on the side of a droplet of tin. The laser energy is 30 mJ, the spotsize is 66 µm, and the droplet diameter is approximately 2mm. The location of the laser on the target is indicated by a blue cross. As the laser is translated upward, the thickness of the liquid film decreases as the laser will move from the thick droplet to the thin liquid layer. From left to right: in the first image the laser is located on the droplet. The second image shows a breakup of the crown as the laser is translated upward. The third image shows a large ligament below the laser location and a large amount of ejected droplets.

4.3 Results of Target 3

The last and third set of experiments were performed with target 3. Most notably, the orientation of the target is rotated 90°, tilting the target surface horizontal. This change in setup can be seen in section 6.1. The laser has an energy of 5 mJ with a spotsize of 66 µm. In figure 4.4 the images of the substrate and laser induced plasma spot are at the top of the figure, the bottom consists of a schematic presentation of the same scene. In the schematic, the substrate is presented by a gray layer, the laser as a red beam, and the liquid tin as a blue layer. The channel present at the edges of the tables is filled with tin as depicted by the blue color. In addition, the location of the channel is approximated by observation of the liquid jet from the images on top. The global location of the laser is evident from the resulting damage to the top layer after experimentation. In figure 4.4(a) the laser spot, visible by the light emitting plasma, is located on the table of the target. No jet or crown is visible. Beginning at (a) and ending at (f), the laser location is shifted from left to right over the channel location. At (b) the laser nears the edge of the channel, resulting in a small jet forming in the channel directed away from the laser spot. In (c) and (d) this jet grows in size as the laser enters the channel. In addition, the jet moves from an angle of approximately 45 deg with the surface to an upright position. Being completely upright in (e) as the laser location is slightly to the right of the center of the channel. In (f) the laser spot is further translated to the right, resulting in a directional splash in the channel away from the laser spot.

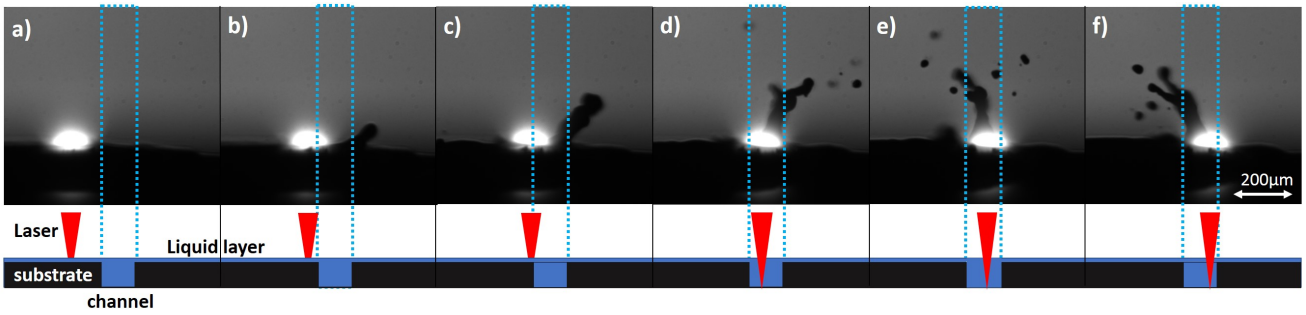

Figure 4.4: Laser impact on a thin liquid tin layer on the standard target. The laser has an energy of 5mJ and a spotsize of 66µm. The laser location is visible as the plasma created by the laser emits light. The laser is translated from left to right over image (a) to (f) over a channel at the edge of the tables. In the lower half of the figure a schematic is given of the relative laser and channel location (laser not to scale). As the laser nears the channel a ligament is formed directed away from the impact zone. This ligament increases in size and as the laser reaches the channel, the ligament will stand up straight (as seen in (e)). In (f) the laser surpassed the half way point in the channel and the resulting ligament swings the other way, redirecting itself away from the laser impact zone.

Visual evidence on the targets after experimentation, as damage on the substrate is visible at low layer thickness areas, supports the suspicion that the crater formed by laser impact reaches all the way down to the substrate. An example of damage visible on the target after experimentation is given in figure 4.5a.

The damage on the target due to laser impact was visible on the target after experimentation. An example of this damage can be seen in figure 4.5 after the tin has solidified. In figure 4.5a the slightly darker gray region around and on the tables is a thin layer of tin. The lighter gray, best visible at the leftmost edge, with small pores in the surface is the underlying tungsten substrate. The laser was translated along the line pointed out by the left red arrow. This shows a removal of the wetted tin surface along the laser path. In the channels a removal of the tin from the surface is also visible as a darker patch reveals the empty reservoir. In figure 4.5b shows the same damage of the laser on a thick tin layer after it has been solidified. The thick layer shows signs of heavy use as indicated by the red arrows, which show the path of the laser. This line is only superficial. The targets were left to solidify in medium vacuum under no laser impact for at least 30 minutes.

(a) Damage of the laser spot on a target with thin liquid tin layer after experiments, the path of the laser during experimentation can be seen. The arrows indicate the laser path

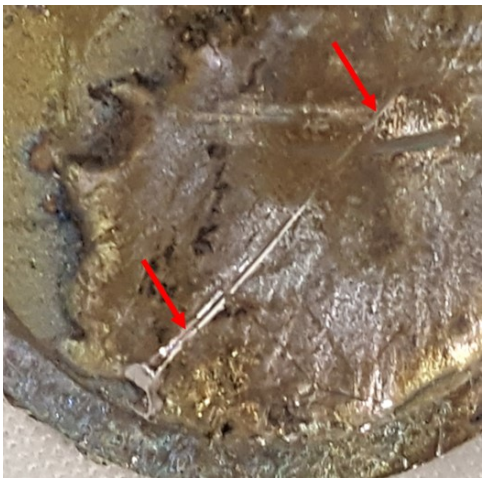

(b) Damage of the laser spot on a target with thick liquid tin layer after experiments, the path of the laser during experimentation can be seen. The arrows indicate the laser path

Figure 4.5: Damage of the layer and substrate due to laser impact on the targets after experimentation

5 Discussion

We suspect that low layer thickness significantly influences the splash around a certain unknown threshold. In figure 4.2 repeated laser impact on a liquid layer is observed. Figure 4.2 indicates a reduction of the liquid layer over a total of 3600 impacts. This reduction may point out a flaw in the design as the liquid layer is unable to fully regenerate and equilibrate to the original condition before the next laser impact. Figure 4.3 shows 3 laser impacts on the same target. This hanging droplet has a continuously changing film thickness. While the laser translates upward the film thickness decreases, as well as the shape of the splash being radically different. For a larger film thickness, a crown is seen with ligaments and secondary droplet generation. As the liquid layer decreases in thickness (by moving the laser spot upward over the liquid surface layer of the droplet edge), the crown starts to break up. At a certain critical layer thickness, the crown of the impact breaks up and only a spray of droplets remain. Assuming the layer thickness at the impact spot of the laser is constant over the surface of the laser spot, the crown rapidly breaks up around a critical layer thickness of 200 μm. This value can be influenced by energy, with the expectation that for higher energy the critical layer thickness increases.

In figure 4.1(a) the spot is presumably located in a valley between pillars. This is based on the assumption of a thicker liquid layer resulting in a crown, and a thin liquid layer resulting in a broken up sheet and droplet spray. The valleys contain a larger amount of liquid tin due to surface tension and meniscus formation. In contrast, the amount of tin on the surface of the target was presumably not enough to cover the peaks, creating a very thin layer of tin (or in extreme cases, no tin at all) on the pillar peaks. We suspect that in figure 4.1(e) the laser spot is located on top of a pillar and thus no splash is visible. In figure 4.4 the thin layer showed a spraying of tin, indicating that the pillar top has an even thinner layer of tin, or no tin at all. Unfortunately damage to the pillar was not checked.

One observation of splash direction can be best seen in figures 4.1(c - g) and in figure 4.4. In figure 4.4 this effect is most visible. As the laser spot is moving toward the larger layer thickness, a directional jet is seen to form. This jet is formed from the larger layer thickness away from the laser. In figures 4.1(c) two ligaments are directed upward under angle with respect to the normal of the surface, away from the laser spot. In (d) this ligament is under a larger angle. At (f) and (g) the direction of these ligaments are downward, again towards the side of the assumed larger layer thickness. Showing the same effect as in figure 4.4. This effect of directional splashing can be attributed to the change in surface geometry. In figure 4.1 this geometry change is in the form of pillars and valleys, in figure 4.4 the geometry change is in the form of a small, deep channel. Furthermore, the channel showed a steerable splash depending on the target geometry and laser location. However, the layer thickness also may play an important part in the splash characteristics in these cases, as in both figures the geometry and layer thickness changes. These two parameters cannot be uncoupled using this data, resulting in a stalemate.

These results pave the way for an answer to the original research question posed in section 1. As the splash is affected by the geometry of the target and can be directed by the geometry and laser location, we suspect that a more sophisticated design will at least be able to reduce splashing. Also, as damage to the substrate is observed with thin layers, it is not recommended to increase laser energy or decrease the layer thickness. One path forward may be the use of a narrow deep bath, this showed a steerability of the splash. However, more research is needed to solidify this claim.

Part II

Analysis of Secondary Droplets

6 Experimental Method

6.1 Experimental Setup

Much of the existing setup of the Experimental Setup A is reused in the second phase of the experimentation. This section solely focuses on the changes compared with the setup of the first phase of the project.

With the addition of an aperture after the beam expander lenses the laser spot is made circular. A more substantial change is the orientation of the target, which is placed horizontally. This results in the beam path travelling in the upward direction (out of the paper) in the beam tower depicted in the cut-out of figure 6.1. After the beam tower the focus lens is placed and directly above the vessel the beam is directed downwards to impact the target in its new orientation. Another difference is the liquid layer on the target. In addition, a hydrogen flow is used to combat re-oxidation of the target after laser impact. Via a can of grade N2.0 hydrogen and a screw valve a hydrogen flow is introduced in the vessel, indicated by a rise of pressure of approximately 0.05 mbar.

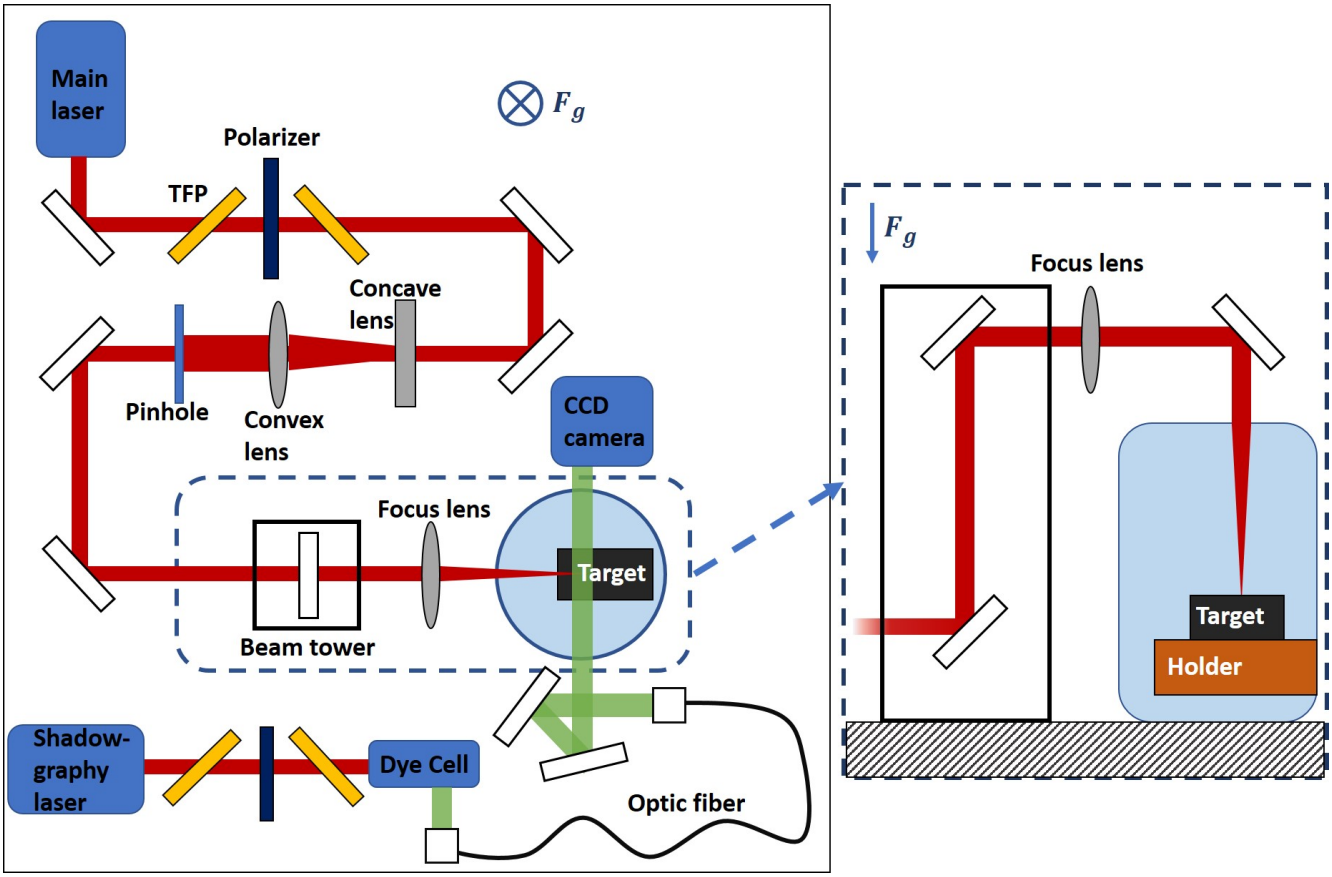

Figure 6.1: A schematic representation of the top view of the experiment including the shadowgraphy setup, target, and main (YAG) laser. The laser beam is represented by the red path starting at the main laser and terminating at the target. The setup consists of a main laser, a set of TFP's and a polarizer, a concave and convex lens, a pinhole, beam tower, focus lens, target and target holder, the vessel, a shadowgraphy setup, and a CCD camera. The cut-out shows the last leg of the beam path entering the beam tower. This is a side view showing the laser path being redirected to enter the vessel at the top. The target and target holder are placed horizontally.

The laser profile in setup B is measured using an alternative focusing lens, due to safety and practical reasons. The alternative focusing lens is inserted between the pinhole and the beam tower. In figure 6.2 the beam profile is given. The white cross represents the orientation of the major and minor axis and the green circle represents the measured FWHM beam spot. The spot size is 66 µm. In figure 6.3 the relative intensity Gauss curves along the major and minor

axis are given. The addition of the pinhole eliminates the ellipticity seen in the profile of Part I (see figures 3.2 and 3.3). In the relative intensity Gauss curves, at the edge the slight bump is decreased with respect to the curves of Part I.

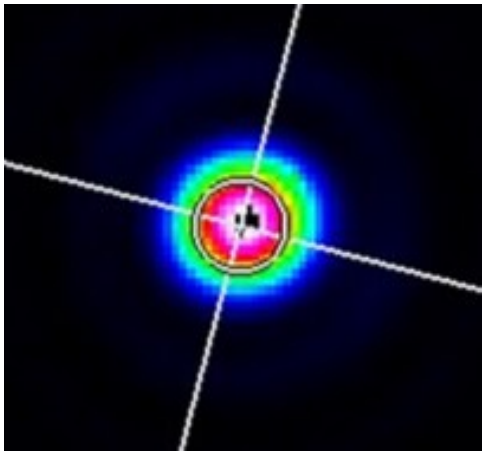

Figure 6.2: The 2D beam profile as measured by the CCD camera after an alternative focusing lens for Part II. The profile is at the focus point of the lens.

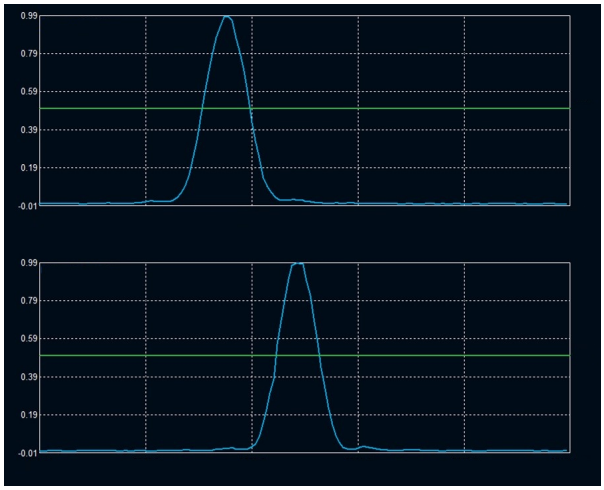

Figure 6.3: The relative intensity curves along the major and minor axis from top to bottom for the laser beam used in Part II.

6.2 Target Used in Experimentation

6.2.1 Target 4

Target 4 is a flat table target, created by Philips Dunlee by means of SLM. The surface roughness is reduced by EDM done at the EPC. Wetting of the target is done by DIFin the vacuum induction oven described in 3.3.3. After wetting, a large amount of tin is deposited on top of the wetted surface, creating a droplet of tin on the surface 1.5 ±0.5 mm thick. In figure 6.4 the target is given before experimentation. The shiny surface is the tin in liquid form (a reflection of the camera is seen in the tin), the two moats are at the top and bottom side of the tin layer. The clamping ring of the target holder with three screws is visible around the target. The black hue on the target (best visible in the moats) is a rubber deposition from a rubber ring used in earlier experiments. The tin layer is rubber free as the color indicates.

Figure 6.4: Target 4: flat table target with a thick layer of tin

6.3 Image Processing using MatLab

Since the output of the experiments are a large set of images per experimental run, the processing of these results are done using MatLab. For this purpose a MatLab script was written to detect the droplet diameter and number per image. Not all droplets are counted by the code since some droplets are below a resolution limit, some have too little spacing

between the ligament and the droplet itself, or droplets may be out of focus. To ensure the droplets are detected that are in focus, just formed from a ligament, and large enough to accurately measure, a selection procedure was put into the code. However, before this procedure was invoked, several other processes are executed. The exact code used is included in the replication package.

Firstly the code reads in the images from the current folder, after which a background is selected by the user. This background is then used to perform a background subtraction on the images, revealing the difference between the background and the current image. This difference is the splash and possibly secondary droplets from the laser impact. The difference image's contrast is subsequently improved and a binary image is formed using a multi thresholding tool using Otsu's method [54, 55]. With this binary image the locations of all droplets are measured on the image and stored. Then returning to the original image, a local region of interest is selected around each detected droplet. For each droplet the gray value profile is measured as well as the normalised gray value profile, the maximum gradient of this profile, the contrast difference on gray value scale of 256, and the FWHM of the normalised profile. For each droplet these 5 values are taken in the horizontal and vertical direction along the mid point of the local region of interest around the droplet. If the droplet is centered in the region of interest, is round, and has no closely adjacent objects, the 5 values' horizontal and vertical counterparts are a >90% match. Then each droplet with their respective values for the maximum contrast, maximum gradient, and FWHM are subjected to a selection procedure. Droplets that are in focus and above the resolution limit are selected, by imposing some thresholds for the maximum contrast, maximum gradient, and the FWHM. This imposes a resolution limit on the droplet diameter based on smallest droplet that can be detected, and a different resolution limit to the time based on the spacing between a droplet and ligament. The values chosen for the analysis used in this project are given in table 6.1

Table 6.1: Selection criteria and their threshold values for the MatLab code to select droplets.

criteria	**droplet passed if**
contrast difference	> 55 [gray value]
maximum gradient	> 8 [gray value/pixel]
FWHM	> 5 [pixel]

After the droplets have passed the selection, the actual diameter is measured by taking the width of the gray value profile at 61% of the contrast difference [56]. This number is chosen to account for the diffraction of light around the droplet to measure its real diameter. A block diagram of the MatLab code is given in figure 6.5. To ensure the correct selection and detection of droplets a manual check of droplet diameter and selection is done in the following section.

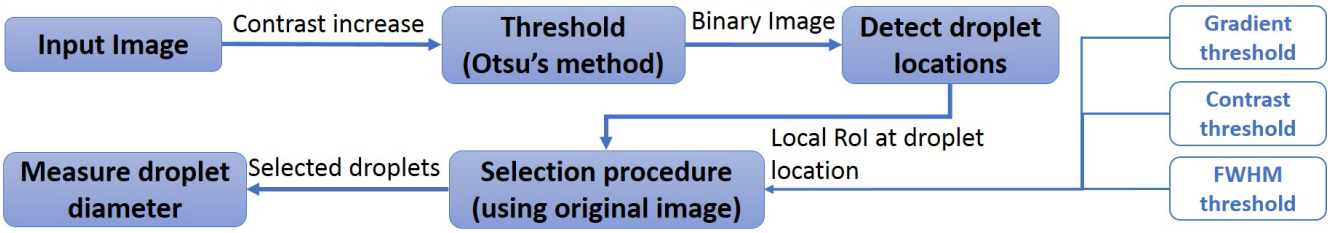

Figure 6.5: Block diagram of the MatLab code used to detect, select, and measure droplets for the analysis of secondary droplets.

6.3.1 Sensitivity Analysis

Since the image processing steps used by the MatLab script extensively use thresholding to detect the desired features, an analysis is done to determine the robustness of the code. Most notably, the droplet detection is subject to rigid criteria such as a region of interest, droplet gray value, minimum pixel width of the droplet, and sharpness of the transition of gray values. In figure 6.6 an image of a splash is given with droplets not fulfilling the criteria (table 6.1) marked by red squares and droplets that passed the criteria in green squares. For a typical droplet out of focus the histogram is given on the left, showing a lower gradient on the profile and a typical droplet in focus is given on the right, showing a large gradient at the edge and a plateau in the middle of the profile. The selection criteria satisfactorily detect droplets in focus

and measure the real diameter using the profiles seen in figure 6.6 at 61% of the contrast difference. The measured and selected droplets seen in figure 6.6 have good agreement with the manually measured and selected droplets from a similar splash. The agreement is defined as sufficiently good when nine out of ten droplets are selected and measured according to the sampled manual measurements. More splash images can be found in the appendix.

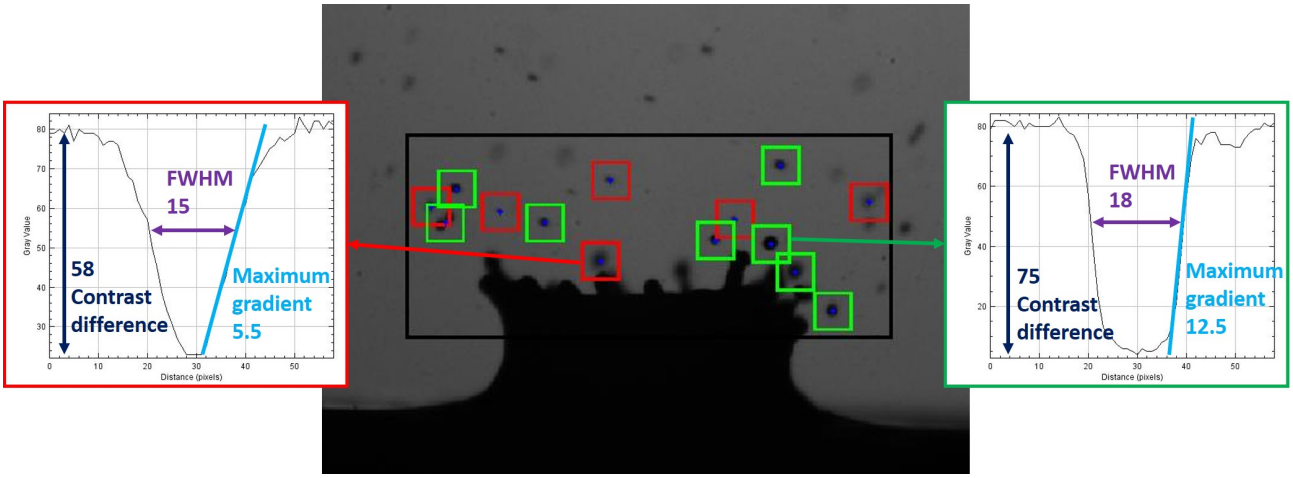

Figure 6.6: A splash from a 20 mJ laser pulse 90 µs after laser impact. The black region is the global region of interest where all droplets are first detected, the red squares indicate the droplets not fulfilling the selection criteria of table 6.1, and the green squares indicate the droplets that do fulfill the criteria. On the left is a typical gray value profile of an out-of-focus droplet. On the right is a typical gray value profile of an in-focus droplet. Inside these two cut-outs, the contrast difference, FWHM, and blur are represented by a dark blue, purple, and light blue line, respectively. The contrast difference of the left cut-out is 58, the width is 15 pixels, and the maximum gradient is 5.5. The contrast difference of the right cut-out is 75, the width is 18 pixels, and the maximum gradient is 12.5.

7 Results

In this section the results of the fragmentation experiments of the laser ablation splash on thick liquid tin films are given and discussed. The target used is target 4 described in section 6.2. During experimentation the target is refilled with tin as needed in open air.

7.1 Qualitative Behaviour of Droplet and Laser Impact Splashing

To compare splash characteristics of the thick layer for a droplet impact with a laser impact, two overviews of the resulting splashes for each case are given in figures 7.1 and 7.2, respectively. More images of laser impact splashes are given in the appendix.

An overview of the thick layer splash by droplet impact is given in figure 7.1 with We = 2207, Re = 12770, and Oh = $3.68 \cdot 10^{-3}$. Here a series of images show the incoming droplet just before impact into the liquid layer, the evolution of the crown both in height and width, formation of ligaments and secondary droplets, the devolution and redeposition of the crown, and lastly the formation of a jet. Also visible is the crater formed by the pressure difference of the impacting droplet. The times given in this figure are the non-dimensional time as it is defined in equation 2, using the diameter of the incoming droplet of 2.88 mm as D and its velocity of 4.42 m/s as U. At $\tau = 2.5$ a fully formed crown is visible with an outward hanging rim edge. As time goes on the crown rim starts to form in an ever more upright position seen at $\tau = 13.5$. At later times the crown starts to fold inward visible at $\tau = 25.7$, at this point the maximum crown height is also reached. At $\tau = 76.0$ the crown is descended back into the liquid and a primary jet is seen to be forming. This primary jet is at its maximum height at $\tau = 145.1$.

The overview of the thick layer tin splash due to laser ablation is given in figure 7.2, showing time in the non-dimensional time as defined in equation 2 in the top left corner of each subfigure. In the work of J.C.J. Hermens the definition of the velocity (U) and characteristic length (D) is defined as the first measurable velocity of the crown rim and first measurable crown width. The values for U = 27.97 m/s and D = 305.1 µm for this case of 10mJ are kindly supplied by J.C.J. Hermens. Non-dimensional numbers of this impact are We = 3038, Re = 42670, and Oh = $1.29 \cdot 10^{-3}$. Figure 7.2 begins at 0.5 µs after laser impact ($\tau = 0.0$) in the top left image. At $\tau = 0.3$ the crown is clearly visible over the surrounding liquid tin, with several ligaments beginning to form. At later times ($\tau > 1.4$) secondary droplets are seen to fragment from the created ligaments, as clearly seen at $\tau = 6.4$. The crown has a maximum height approximately at $\tau = 11.9$ and after this time starts to devolve and widen further. This widening can be seen in the images of $\tau = 27.5$ to $\tau = 45.8$. After the widening and subsequent flow back of the crown into the liquid pool, a rush of liquid into the laser created crater pushes some liquid upward creating a primary jet seen just above the surface at $\tau = 174.2$.

Qualitatively comparing the droplet impact splash of figure 7.1 with the laser impact splash of figure 7.2, we see similarities in the shape of the crown and in the formation of ligaments and secondary droplets. In both cases, the crown forms after impact and has a steep crown growth rate in its early stages, during this stage ligaments are beginning to form. After the early stage and the crown formed sufficiently large ligaments, these are seen to pinch off and form secondary droplets. This process of ligament formation and secondary droplet atomization carries on into the later stages of the splash. After the crown is descended back into the liquid layer a large jet is seen in both cases. The non-dimensional time in the droplet impact case is slightly different from the non dimensional time in the laser ablation case. This can be seen in the last image of both figures 7.1 and 7.2, where the primary jet is seen. In the droplet impact this has a maximum height at $\tau = 142.1$. In the laser impact the primary jet has a maximum height at $\tau = 172.2$. This slight difference is smaller in the lower non-dimensional times as seen in figure 7.1 at $\tau = 3.7$ and in figure 7.2 at $\tau = 3.1$. In both images the splash is directed outward, having an angle between the base of the crown and the left and right most top of the crown. The similar behaviour is supported by the non-dimensional We and Re numbers, as they are the same order of magnitude.

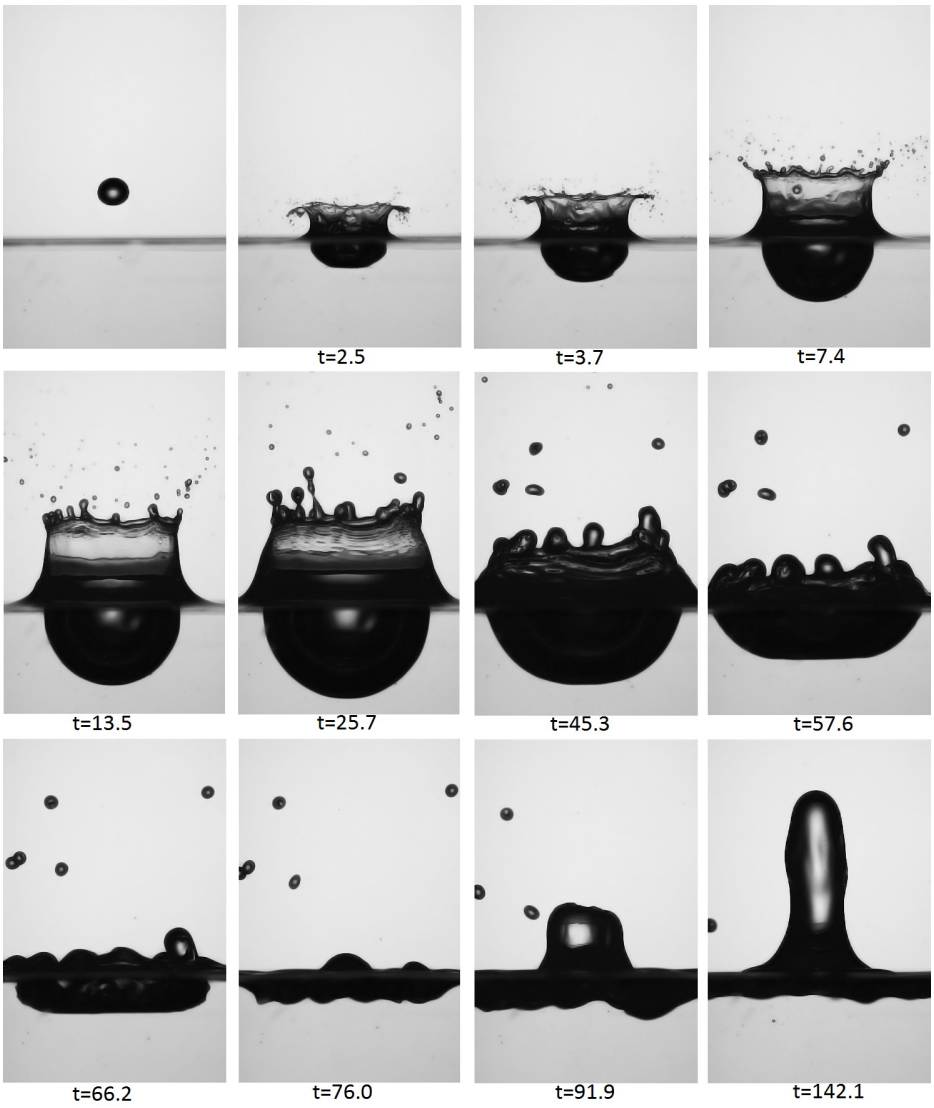

Figure 7.1: A series of images showing an acetic acid droplet impacting a deep acetic acid pool with drop diameter 2.88 mm, drop velocity 4.42 m/s, We = 2207, and Re = 12770. The top left image shows the droplet as it is just about to impact the pool of acid. In following figures a crown as well as an underlying crater is formed after the droplet has impacted. As soon as 3.7 after droplet impact small secondary droplets can be seen atomizing at the ligament edges. At non-dimensional time 13.5 the crown is starting to close in on itself after a rapid crown evolution, in comparison to earlier times the secondary droplets are larger and less numerous. At time 25.7 maximum crown height is achieved and the crown starts to collapse, larger ligaments can be observed at the rim. From time 45.3 to 76.0 the crown is collapsing and the underlying crater is being filled by the surrounding liquid. Large secondary droplets can be seen ejected from the ligaments of the receding rim. From 76.0 a primary jet is formed by the collapse of the crater evolving up to time 142.1 where the jet is at its peak. Figures adopted from [57].

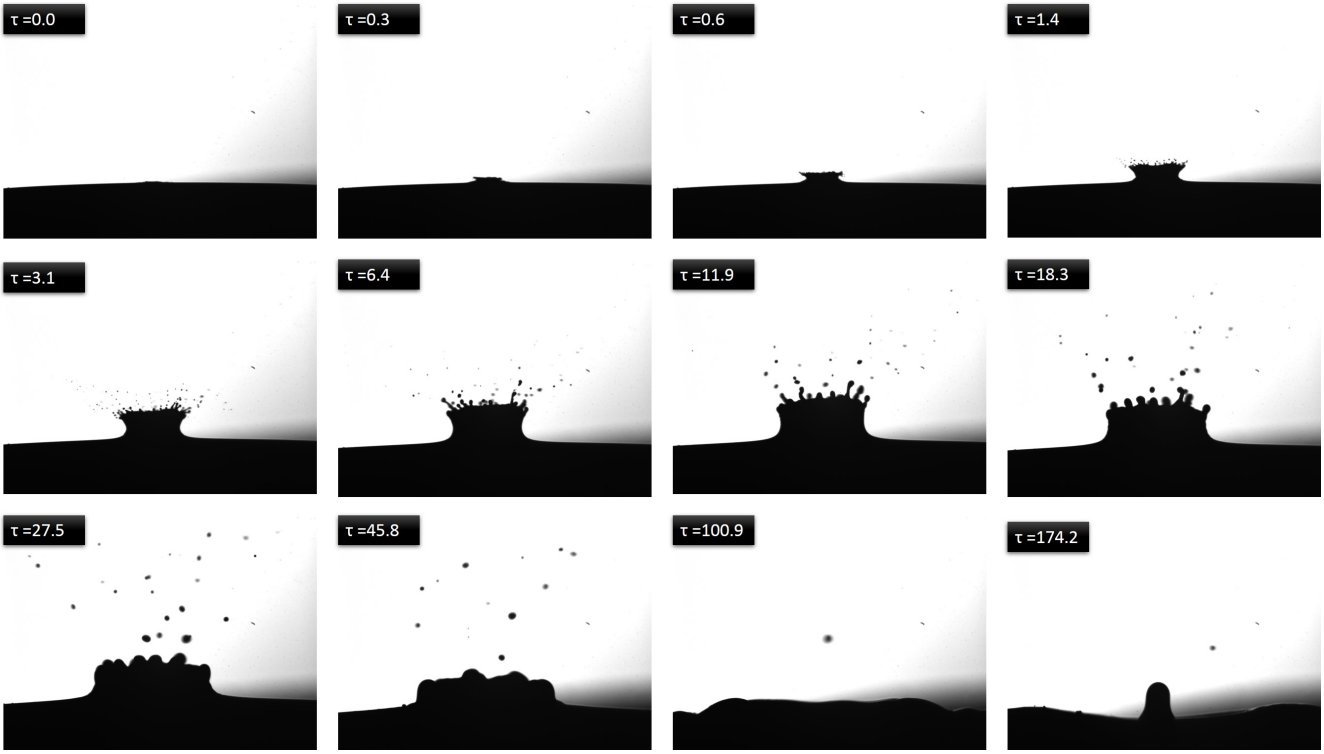

Figure 7.2: An overview of the laser ablation splash in a thick liquid tin layer over time. Each frame shows a different time of the splash, given by the non-dimensional time in the top left corner of each splash frame. The laser pulse used in this case had an energy of 10 mJ, a spot size of 66 µm*, We = 3038, and Re = 42 670. Laser impact is at* $\tau = 0$ *and after this the crown starts to grow up to a maximum height. After reaching this height, the crown starts to fall back into the liquid layer. Finally a primary jet is seen as liquid will rush back.*

7.2 Phase Diagram of Fragmentation Onset

In the analysis of crown sheet fragmentation into secondary droplets, it is important to know where in the parameter space this fragmentation occurs. For this purpose the fragmentation onset of the crown as a function of the laser energy and spot size is observed. This varying of the laser fluence by changing either the laser energy or the spot size will give information about the detachment of secondary droplets from their corresponding ligaments. Firstly, we define splashing as the fragmentation of secondary droplets from their corresponding ligaments on the crown rim. This means that droplets must be clearly be originating from a perturbation of the crown sheet, which will grow into a ligament capable of fragmentation. In the dataset this criteria is often hard to distinguish as each frame corresponds to a new and different splash. For this reason it is hard to determine if a droplet is originating from a ligament, or an anomalous source. For this reason droplets that have just detached from a ligament, with the corresponding ligament still visible, are counted. The exact onset of fragmentation can be considered a region of transition between deposition and splashing. Additionally, the laser may experience relatively high disturbances in its profile at low energies (< 1mJ) and the disturbances in the laser profile can cause the impact to splash, resulting in a difficult task to distinguish deposition, transition, and splashing impacts. Nevertheless, classification is done with the criteria to distinguish the deposition, transition, and splashing impacts that are given in table 7.1 with $N_{avg,drop}$ the number of droplets averaged over all images.

Table 7.1: Classification criteria for the deposition, transition, and splashing impacts for the phase diagram data.

Type of impact	Criteria
Deposition	$N_{avg,drop} \leq 0$
Transition	$0 < N_{avg,drop} < 1$
Splashing	$N_{avg,drop} \geq 1$

In figure 7.3 the phase diagram of the fragmentation of ligaments for the thick layer laser ablation is given. The data used is given as green circles, red triangles, and blue diamonds for deposition, transition, and splashing impacts, respectively. In figure 7.3, the coloured faces represent the deposition parameter space (green), transition parameter space (red), and the splashing parameter space (blue), and the lines represent lines of constant energy fluence. Underneath the diagram 3 images of laser ablation impacts are given. The deposition image shows a stable crown without perturbations along the rim, indicating no formation of ligaments and therefore no secondary droplets. The image is taken from a laser impact with energy 0.20 mJ, spot size 85 µm, and time after laser impact 2 µs. The transition image shows a crown starting to form ligaments. The image is taken from a laser impact with energy 0.50 mJ, spot size 85 µm, and time after laser impact 2 µs. The splashing image shows a crown with ligaments and secondary droplets from these ligaments. The image is taken from a laser impact with energy 2.00 mJ, spot size 85 µm, and time after laser impact 2 µs. Also note the difference in crown width and height for the different fluence impacts depicted in figure 7.3. For the lower fluence impact of $3.5 * 10^{-2}$ mJ/cm^2 the crown is significantly smaller (width 150 µm, height 20 µm) than the higher fluence impact of $3.5 * 10^{-1}$ mJ/cm^2 (width 275 µm, height 60 µm). This is expected as more energy supplied to the plasma, increases its expansion rate and causes a sharper pressure difference locally. For the following experiments all impacts are in the splashing regime as secondary droplets are analysed.

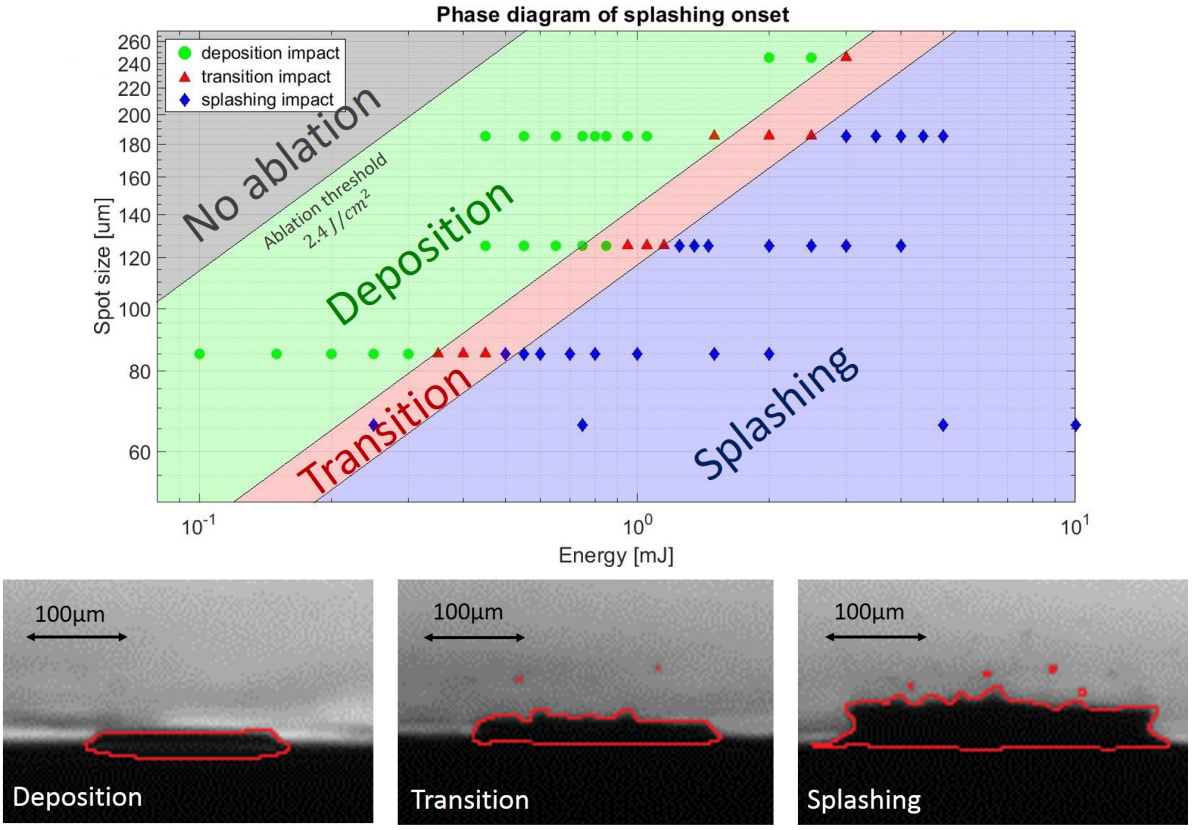

Figure 7.3: (top): Phase diagram of the onset of fragmentation with spot size on the vertical axis and energy on the horizontal axis. The data taken by several spot sizes and energies are depicted as green circles, red triangles, and blue diamonds for the deposition, transition, and splashing impacts respectively. The different regions are coloured accordingly the symbols: Deposition in green, transition in red, and splashing in blue. The linear graphs are lines of constant energy fluence with higher fluence from the ablation threshold toward the splashing region. The transition region is between $0.16\frac{\mu J}{\mu m^2}$ *and* $0.24\frac{\mu J}{\mu m^2}$*. (bottom): Three images of crowns corresponding to, from left to right, a deposition impact, a transition impact, and a splashing impact at* 2µs *after laser impact and a spot size of 85µm. From left to right the laser energies are 0.20 mJ, 0.45 mJ, and 2.00 mJ, respectively. Scale bars are inserted into the figures.*

7.3 Secondary Droplet Distribution

During the analysis of the secondary droplet count and size distribution over time, a MatLab script is used to count droplets above the crown of the main splash. This script is detailed in section 6.3. The first part of the splash from 0 to 100 µs, shows the onset of secondary droplet fragmentation. The second part of the splash is from 100 to 300 µs. From 0 to 100 µs the splash is seen to evolve much faster than from 100 to 300 µs. Therefore, first part of the splash has a time resolution of 2 µs and the second part of the splash has a time resolution of 10 µs. The division is done to reduce the amount of data.

In figure 7.4 the droplet size distribution of a laser ablation splash by a 5 mJ, 10 mJ, and 20 mJ laser pulse is given. The spot size is 66 µm for all three cases. A histogram plot is given of the amount of droplets counted in each time step with a certain droplet radius. The total amount of images per time step is 150 for 5 mJ and 2 0mJ and 300 images for 10 mJ. In the figure an average droplet count per image is given. In figure 7.4 the vertical axis gives the droplet diameter in µm. On the horizontal axis is the time in µs from 0 to 100 µs for the left part and from 100 to 300 µs for the right part. The colormap shows the average amount of droplets detected per image for each droplet diameter range at each timestep on a logarithmic scale. Note that for the 5 mJ case the scale of the colormap is significantly lower than for the 10 mJ and 20 mJ cases.

The 5 mJ distribution of figure 7.4 (top distribution) shows a low average droplet count per image. Some droplets are detected as early as 6 µs after laser impact, the larger distribution begins approximately at 20 µs. The distribution at 200 µs starts to show lower droplet count and continues to decrease in counts from that time forward.

The 10 mJ distribution of figure 7.4 (middle distribution) shows the first droplets counted at 10 µs. At 150 µs the droplet count starts to decrease significantly and continues to decrease over time from this point in time forward. At 200 µs large droplets are counted with a diameter of 90 µm. This count continues to 300 µs.

The 20 mJ distribution of figure 7.4 (bottom distribution) shows the first droplets counted at 8 µs. The larger distribution begins approximately at 20 µs and is centered around 20 µm. From 50 µs on out the distribution shifts to 40 µm. The distribution is centered around 40 µm from 70 µs to 150 µs. At 200 µs the distribution formerly centered around 40 µm has a very low droplet count. A secondary distribution appears centered around 9 0µm at 150 µs as well. In total, two steps in droplet size can be seen. The first being at 60 µs and the second at 150 µs.

From the distributions of figure 7.4, the 20 mJ laser impact case, most clearly shows two different distributions. The first distribution consisting of droplet diameters in the range of 15 µm to 75 µm in the time range of 20 µs to 200 µs. The second distribution consisting of droplet diameters in the range of 70 µm to 110 µm in the time range of 150 µs to 300 s. We suspect prompt splashing to be responsible for the first distribution and delayed splashing for the second distribution. The difference in dominant parameter for the prompt (viscosity) and delayed (surface tension) splashing, in tandem with the changing crown sheet thickness over time, allows for radically different mean droplet diameter. In the 10 mJ case the delayed splashing is less visible in the distributions. The 5 mJ case shows no sign of delayed splashing in the distribution. An explanation of the lack of delayed splashing for the 5 mJ case may be the lower energy. The 5 mJ laser impact is suspected to not supply enough energy to the system for ligaments to grow large enough to allow pinch off and create secondary droplets in the descending stage of the crown.

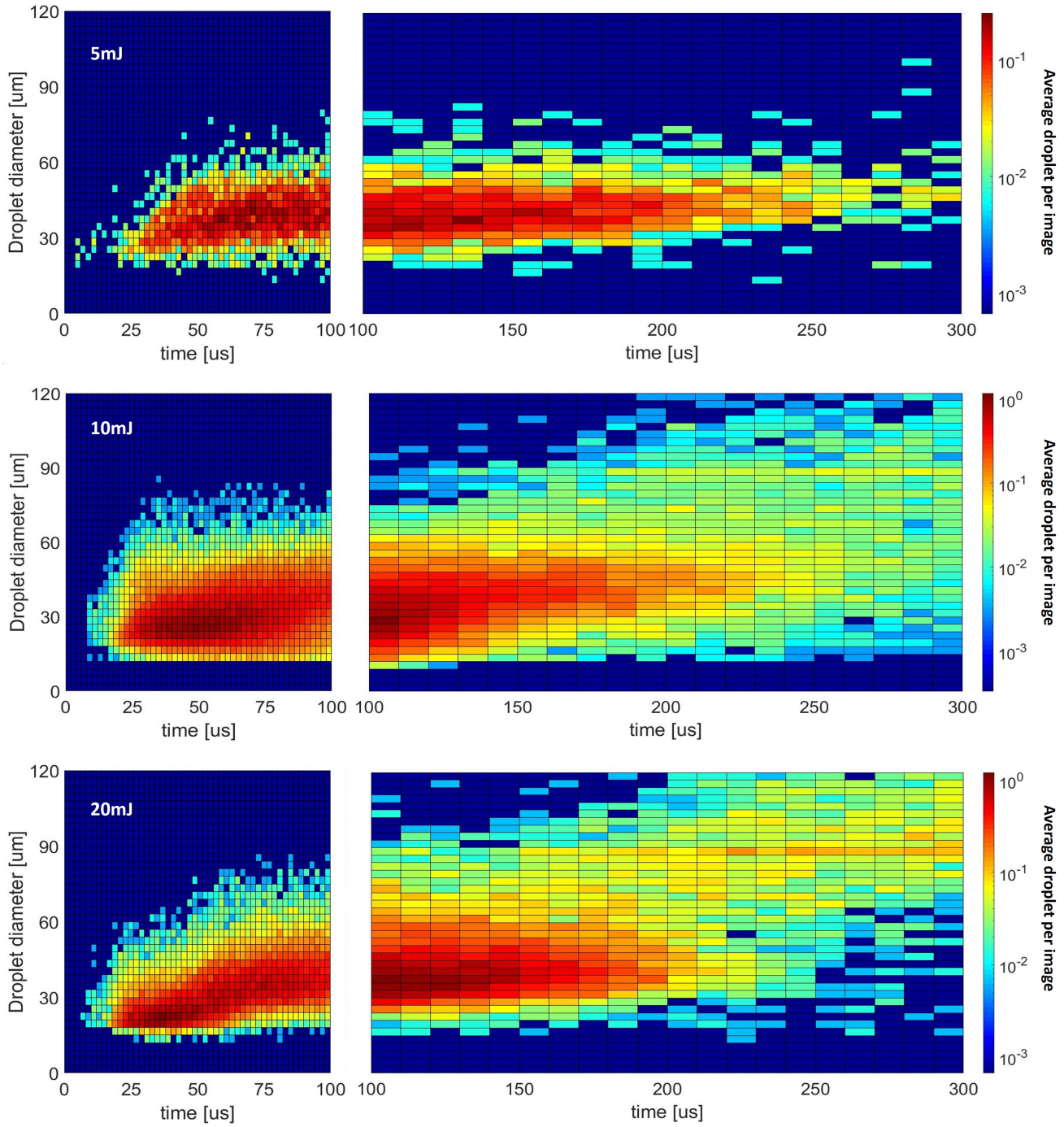

Figure 7.4: Droplet diameter distributions over time for three energies. On the horizontal axis is the time, on the vertical axis is the droplet diameter with steps of 3 µm. The colormap shows the count of detected droplets falling into the droplet and time range. The droplet count is averaged over all processed images per timestep. The top distribution is for a laser energy of 5 mJ, the middle distribution for a laser energy of 10 mJ, and the bottom distribution for a laser energy of 20 mJ. The left parts of the distributions show the beginning of the splash from 0 to 100 µs with a time step of 2 µs. The right parts show the second part of the splash from 100 to 300 µs with a time step of 10 µs.

7.3.1 Gaussian Droplet Distributions, Mean Droplet Diameter, and Local Rim Velocity

In this section, droplet diameter probability distribution functions (PDF) are given for 30 s, 120 µs, and 240 µs after laser impact are given. The droplet diameter PDF for these times is fitted with a Gaussian distribution curve as seen in equation 5. Furthermore, the heights of the 5 mJ, 10 mJ, and 20 mJ crowns are supplied by J.C.J. Hermens. The local velocity U of the upward motion of the crown is calculated by taking a moving average of the height data and then taking the gradient. To indicate the behavior of the mean rim diameter over time, $1/\sqrt{U}$ is plotted on the left-hand y-axis, because from equation 6 it follow that the We number goes as $1/\sqrt{U}$ and no other parameters than the velocity are changed. The mean droplet diameter d_{mean} over time is also given.

In figure 7.5 the droplet diameter PDF's and data points are given in the left hand graphs. The $1/\sqrt{U}$ and mean droplet diameter over time are given in the right hand graphs. The PDF's of the 5 mJ impact show distributions for 30, 120, and 240 µs centered around 30, 42, and 42 and 52 µm, respectively. The $1/\sqrt{U}$ over time shows an increase till 125 µs after laser impact. From that time forward a decrease is seen with a small local maximum around 170 µs. The mean droplet diameter sharply rises from 20 µm to 40 µm from 25 µs to 50 s. From 50 µs onward a small increase in mean droplet diameter is seen.

For the 10 mJ case, the PDF's of 30, 120, and 240 µs, are centered around a diameter of 30, 33, and 45 µm respectively. The Gauss fit of 240 µs shows a small shoulder at 75 µm. The $1/\sqrt{U}$ curve for the 10 mJ case shows a gradual ascent from 0 µs to 100 µs. From 100 µs to 160 µs the $1/\sqrt{U}$ sharply increases, peaking at 160 µs. From 160 µs forward a sharp decrease is seen lasting until 200 µs. The mean diameter shows a continuous increase over the full time, with a discontinuity at 100 µs.

For the 20 mJ case, the PDF's of 30 and 120 µs are centered around a diameter of 16 and 40 µm respectively. The PDF of 240 µs has two peaks and located around 42 µm and 90 µm. The $1/\sqrt{U}$ curve shows a gradually increasing trend from 0 µs to 200 µs. After 200 µs it decreases slowly until 275 µs, after this time the curve falls off to zero. The mean diameter shows two sharp increases, the first being from 50 µs to 75 µs and the second from 150 µs to 250 µs.

For all three laser energies, the PDF of 120 µs is shifted toward larger droplet diameters and becomes a broader distribution compared to the PDF of 30 µs after impact. The PDF of 240 µs shows two peaks for the 5 mJ and 20 mJ laser impact. The 240 µs PDF of the 10 mJ case does not show 2 clear peaks, instead a small shoulder on the right hand side of the distribution is seen. A similar shoulder is seen on the 120 µs distribution for the 20 mJ case. At later stages the distributions for the different energies start to deviate much more compared to the initial stage as indicated by the similarity of the 30 µs PDF's and the differences in the 240 µs PDF's for the three energy cases.

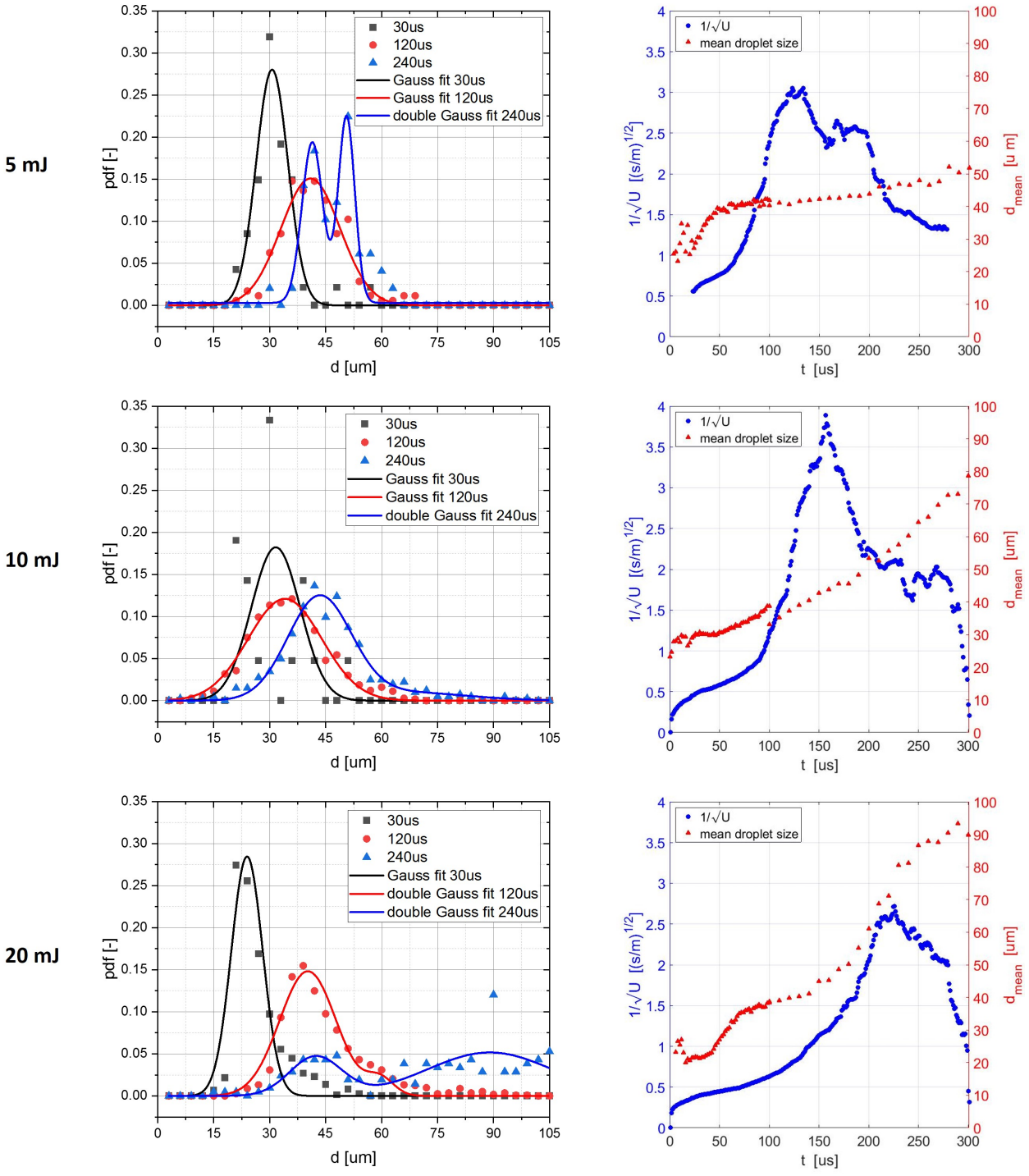

Figure 7.5: (Left): Droplet diameter datapoints and fitted PDF's using a Gaussian fit. Data from 30 µs, 120 µs, and 240 µs are taken. On the horizontal axis the droplet diameter in micrometers, on the vertical axis the PDF. For 30 µs and 120 µs a single peak is fitted, for 240 µs a double peak is fitted. (Right): The inverse of the square root of the upwards crown rim velocity and the mean droplet diameter. U is the upwards crown velocity given in m/s. On the left vertical axis the inverse of the square root of U is given. On the right vertical axis the mean droplet diameter is given in micrometer. The horizontal axis gives the time in microseconds. From top to bottom the PDF's, inverse of the square root of U, and mean droplet diameter are given for a laser impact of 5 mJ, 10 mJ, and 20 mJ respectively.

7.3.2 Initial Weber Number

As described, the initial stage of the splashes by the three different laser energies show similarities in the fitted PDF's. In figure 7.6 the PDF's of each energy at 30 µs after impact is given in one figure. The peaks of the fitted curve for 5 mJ, 10 mJ, and 20 mJ are centered around 30 µm, 27 µm, and 23 µm, respectively. Furthermore, in the initial stage of the splash, inertial forces dominate. The initial Weber number is defined as given in equation 3 with the U and D from the MSc work of J.C.J. Hermens. This Weber number is valid only in the early stages as the U and D are derived from the first measureable crown velocity and the first measurable crown width. Both of these are taken several microseconds after laser impact. In figure 7.7 the Weber numbers of the three laser energies of 5 mJ, 10 mJ, and 20 mJ are given with the most probable droplet diameter taken from figure 7.6. The Weber number in figure 7.7 is calculated by taking the initial U and D provided by J.C.J. Hermens and giving the density and surface tension a value of unity. The error bars seen in the vertical direction are based on one bin size of the data which is 3 µm. The error bars in the horizontal direction are calculated based on the error of the velocity U and the diameter D. The error of U is assumed to be 10% of its value, the error of D is assumed to be 5% of its value. The red line represents equation 6 with h = 15.4 ±1.5 µm. As seen in figure 7.7 the fit of equation 6 has good agreement with the data.

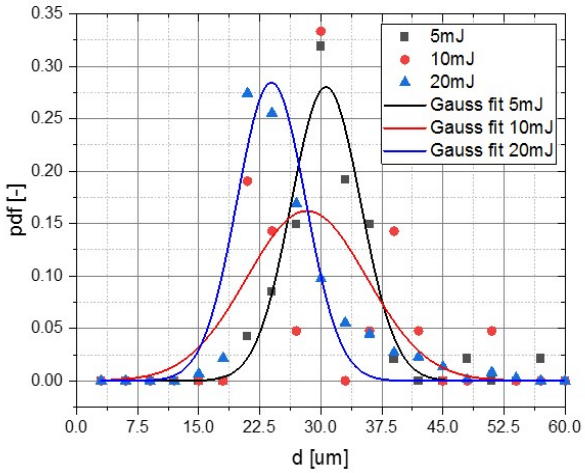

Figure 7.6: Fitted probability density functions and data points for 5 mJ, 10 mJ, and 20 mJ at 30 µs after laser impact. On the horizontal axis the droplet diameter is given in micrometers, on the vertical axis the probability density function is given.

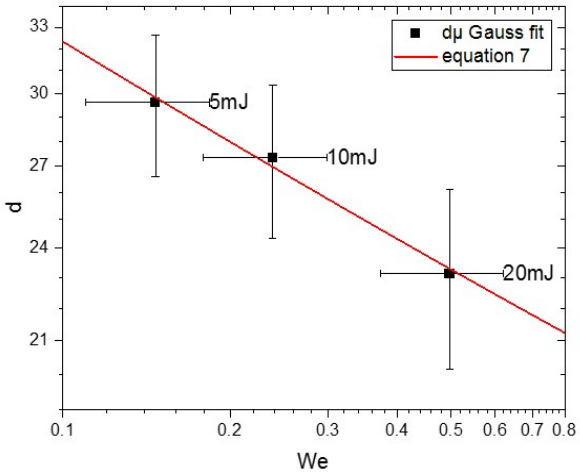

Figure 7.7: A log-log scale graph of the most probable droplet diameter for laser energy impact of 5 mJ, 10 mJ, and 20 mJ at 30 µs after laser impact and their Weber number. Equation 6 is fitted through the points showing a straight line. On the horizontal axis is the Weber number, on the vertical axis the most probable droplet diameter. The laser energy of the corresponding data point is given in the figure next to the data points.

8 Discussion

The onset of the formation of secondary droplets is depicted in figure 7.3, here the regions are given for splashing, transition, deposition, and no ablation. The ablation threshold is taken as a constant fluence from literature. The splashing threshold is suspected to be dependent on the fluence, therefor, the transition between regimes are along lines of constant fluence. As seen in figure 7.3 the transition splashes show good agree with the transition region. However, some splashing impacts are within the transition regime indicating a too small sample size. This may point toward a splashing threshold dependent on more than only the laser fluence. By applying equation 7 more laser energy per surface area, e.g. fluence, results in a larger expansion rate. This will in turn increase the pressure differences in the liquid layer and cause faster upward growing crown to form. The larger the pressure difference, the higher the initial upward crown height growth rate and secondary droplet generation.

The difference in droplet distribution for laser impact for the examined energies of 5 mJ, 10 mJ, and 20 mJ are partly consistent with the expectations found in droplet impact literature of figure 2.11. This states that for larger Weber numbers, the most probable secondary droplet diameter shifts towards smaller diameters and the distribution becomes narrower. The shift toward smaller diameters is exactly seen in the laser impact data for each laser energy at 30 µs after impact for initial Weber number. The initial Weber number is relevant to the comparison of droplet and laser impacts, since the initial energy transfer differs for these impacts. After the impact, the fluid dynamics will be very similar as seen in figures 7.1 and 7.2. Furthermore, the crown height growth rate is used to relate to a local Weber number as it scales with the velocity U. This results in a direct relation between the crown height growth rate and the local Weber number for the crown. As the growth rate increases, so does the Weber number. The largest growth rate is seen in the beginning stages of the splash (0 to 50 µs), consistent with narrow secondary droplet size distributions centered at small droplet diameters. For later times after ablation (50 to 150 µs) this growth rate is smaller and a broader droplet size distribution centered around larger diameters is seen. Both are during the prompt splashing regime. From this we can conclude that the droplet impact case and laser impact case are comparable in the secondary droplet distribution dependence on local Weber number for prompt splashing.

Furthermore, the several peaks in the fitted function of later times in figure 7.5 are proof of a secondary process of droplet formation. The first being prompt splashing as the crown continues to ascend, the second being delayed splashing after the crown reaches its maximum height and starts to descend into the layer. This second distribution peak is most visible in the 20 mJ case for 240 µs after laser impact, where two peaks are visible. In this case the crown has reached its maximum energy and delayed splashing may be the dominant factor creating the second peak.

Figure 7.7 shows the initial Weber number, for later times the distributions do not show this relation. This may be due to different fluid dynamics forces becoming more dominant as the splash grows.

In figure 7.7 equation 6 is fitted through the most probable diameter taken from the fitted curves of figure 7.6. The fit shows good agreement with the data, indicating that the relation between the most probable droplet diameter and the initial Weber number indeed follows the same dependency for the laser impact case as in the droplet impact case. However, the case of 10 mJ shows no agreement with the data points, the exact reason for this may be the difference in back lighting conditions during testing. More experimentation is required to mitigate this problem or identify its cause. Furthermore, in equation 6 the d actually represents the rim diameter. This is strongly connected to the ligament diameter as it is created from the rim. In turn, the ligament diameter imposes restrictions on the secondary droplet ejected from this ligament. Therefore, the rim diameter influences the droplet diameter ejected from that rim. It is, however, not known what the exact relation is between the rim diameter and secondary droplet diameter. In equation 6 the sheet thickness is also present. The sheet thickness for each energy could differ, causing the fit not to fully converge to the data points. In the case of the fit, one value for the sheet thickness is used as a prefactor. Even with the unknown relation of the rim diameter and droplet diameter and constant sheet thickness, the fit shows remarkable agreement with the data. Therefore, the successful fit of an equation based on droplet impact on the laser impact case shows a similarity and commutability of the two cases. In addition, we suspect that the Weber number is the dominant factor for the secondary droplet diameter.

In all histogram figures (figure 7.4) a discontinuity between the left and right halves can be seen. As the right half of the figure begins there is a slight jump in the droplets counted at this time (t=100 µs). This discontinuity can be attributed to an artefact in the droplet detection algorithm. This artefact presents itself as the splash grows larger and the region of interest does not detect any droplets anymore, due to the fact that it does not reach above the crown rim or extends

too low above the crown rim. To combat this effect, the region of interest of overall droplet detection is chosen slightly larger for the later stage of the splash (100 μs < t < 300 μs). This larger region of interest causes more droplets to be detected from the onset of use at 100 μs causing a slight discontinuity in the histogram at that point. This can be solved by adjusting the code to gradually grow the region of interest above the crown rim to match the change in height and width of the crown. Due to time constraints this feature was not implemented in the code and figures.

A lower droplet count is expected and observed in figure 7.4 for the lower energies in contrast to higher energy. As seen in figure 7.3 all are securely in the splashing regime. Due to limitations in the script these tiny droplets seen at the transition from deposition regime to splashing regime in figure 7.3-c are not detected. Furthermore, the classification of a deposition, transition, and splash impact is based on the visible droplets originating from the crown. Droplets out of focus of the camera or smaller droplets may be invisible in the images taken. This will allow a splashing impact to be classified as a transition or deposition impact.

Another artefact of the code, only visible due to the log scale on the colormap of the histogram figure, is the detection of droplets below the resolution limit in droplet diameter, and the detection of some droplets before secondary droplet ejection by the ligaments. Some droplets are detected below the thresholds of the code, implying a fallibility's of the selection procedure. This is caused mainly by small debris on the surface of the liquid layer in the background image. Most debris was observed to be present in the data of the 10 mJ laser impact. As the code uses background subtraction, the debris is suspected to be counted as droplets. This happens in approximately one image per 30 images. In figure 8.1 the amount of falsely detected droplets is depicted by the green squares drawn. The black rectangle is the region of interest around the crown. To prevent these false positives the liquid tin layer on the target must be devoid of any debris on the surface.

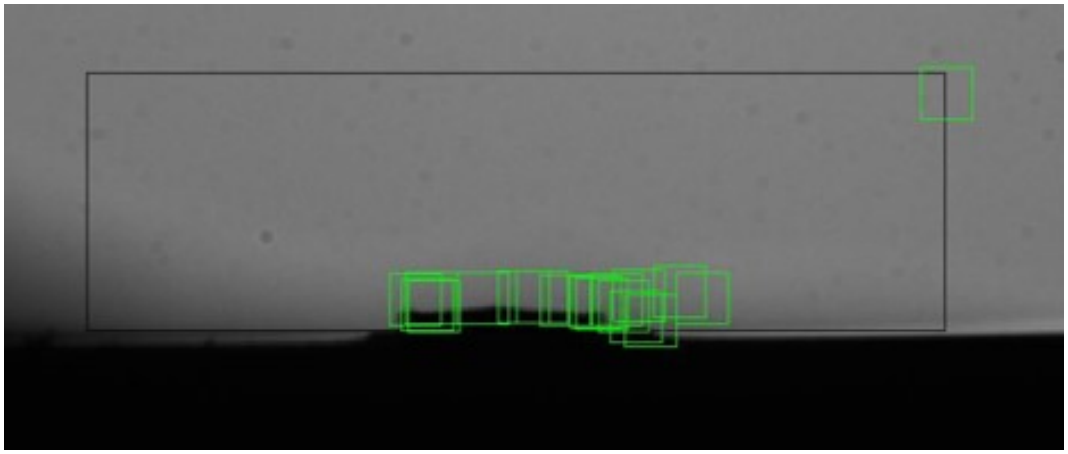

Figure 8.1: False droplets detected by the code. The green squares are drawn around detected droplets. The black rectangle is the region of interest around the crown. As no droplets can be seen in the green squares, the code falsely detects droplets.

Relating back to the research question for this part, the commutability of the literature of droplet impact with laser impact is partly given in the results presented. However, droplet impact and laser impact is not fully proven to be commutable and further research is necessary. The two cases are highly comparable and a strong suspicion of commutability is presented. Crown shape, height, and width are studied in detail in the MSc work of J.C.J. Hermens.

Lastly, on a more application based note, investigation of the deposition regime in figure 7.3 allows us to predict a fluence regime where no significant secondary droplet generation is observed. This regime thus represents an interesting parameter space for generation of EUV light. However, these low fluences cannot produce plasma conditions directly relevant for the production of EUV light. It can, however, be used in a pre-pulse capability as the laser in the deposition regime is above the ablation threshold and thus creates a vapour above the liquid tin layer. This rarefaction of the liquid may be used to create a vapour target for the main laser to ionize into a high intensity, EUV-emitting plasma. The main laser would ideally be directed parallelly to the liquid surface, preventing it from striking and splashing the liquid. Further research must be done to verify this method.

9 Conclusions

The results of section 4 show that the geometry of the target has an effect on the splash formation and evolution. Furthermore, the splash direction can be controlled using the geometry and laser location. These findings pave the way to designing a set of target geometries capable of steering the splashing after laser impact. In this project, however, the goal was to find a design to suppress the splash. No such design is found. Furthermore, the effects of the liquid layer thickness and geometry of the target cannot be uncoupled using the results of section 4, requiring more experimentation of controlled liquid layer thicknesses. Some laser impacts show signs of reduced or even no splashing, this results from a very thin liquid layer at these locations. The very thin liquid layer discourages splashing but also does not fully shield the substrate from the laser impact. After impact on a very thin layer, the substrate shows damage. During the absence of a splash or spray together with the observation of damage, we strongly suspect no tin to be present at the laser location. Another conclusion is the sub-par regeneration of the liquid layer during experimentation. The liquid layer shows signs of depletion with repeated laser impacts.

The differences in droplet distribution for laser impact for the examined energies are partly consistent with the expectations found in droplet impact literature. This states that for larger Weber numbers, the most probable secondary droplet diameter shifts towards lower diameters and the distribution becomes narrower. The shift toward smaller diameters is indeed seen in the laser impact data for each laser energy at an early 30 μs after impact following the same Weber number over the here measured range.

for initial Weber number. Furthermore, the crown height growth rate is used to relate to a local Weber number. As the growth rate increases, so does the Weber number. The largest growth rate is seen in the beginning stages of the splash (0 to 50 μs), consistent with narrow secondary droplet size distributions centered at small droplet diameters. For later times after ablation (50 to 150 μs) this growth rate is smaller and a broader droplet size distribution centered around larger diameters is seen. From this we can conclude that the droplet impact case and laser impact case are comparable in their respective secondary droplet distribution dependence on local Weber number for prompt splashing.

Evidence for prompt and delayed splashing is seen the histogram and fitted Gauss curve for 20 mJ, 240 μs after laser impact. The better fit for a two peak Gaussian function, compared to a single Gauss curve, hints toward a difference in splashing mechanisms at play between prompt and delayed splashing for the laser impact case. This effect of a significant delayed splashing droplet size distribution is only visible for the largest applied laser energy of 20 mJ and the droplet count rapidly diminishes for the 10 and 5 mJ laser energy distributions. Therefore, the increase of this effect is expected for larger laser energies.

The classification of deposition, transition, and splashing is made in the form of a phase diagram. The phase diagram transitions are based on the ablation threshold's dependence on laser fluence. This ablation threshold is subsequently obtained from literature. It is suspected that more energy per surface area, increases the initial pressure difference. Larger pressure difference in turn will increase the crown growth rate, ligament formation, and secondary droplet formation.

A possibly interesting regime for EUV light generation is the deposition regime in the phase diagram. Laser pulses in this regime can be used as a rarefaction pulse, creating an alternative to the pre-pulse used in EUV light generation today. However, more experimentation needs to be conducted to verify this claim.

Finally, further research in the dependency of laser energy and spot size of the laser on the distribution and a definition of a local Weber number during the splash may elucidate the commutability of droplet impact and laser impact further. Relating back to our research question concerning the comparison of secondary droplet atomization between droplet and laser impact, a small step in the right direction is taken. In a bigger context, these findings will contribute to a larger basis of commutability of the droplet impact and laser impact crown formation and secondary droplet formation. Once these cases are proven to be commutable, the trove of literature available for droplet impact will also apply to laser impact.

In sum, the main conclusions are, first, that thin layers are not usable for EUV generation directly due to damaging of the substrate, and substrate geometry variation should focus on deep but narrow baths. And second, that droplet impact and laser impact systems might indeed be commutable. Further research into these topics is therefore recommended.

10 Outlook

For future research a systematic target design can be tested and iterated to find a target geometry capable of reducing the splashing after laser impact. To combat the sub-par regeneration of the layer, a thick liquid layer is necessary. One possible path would be the use of deep, narrow baths.

Further research into commutability of the droplet impact and laser impact splashing, may be the investigation of the splash due to laser impact for a wider range of energies. Specifically, higher energies may show droplet distributions that are clearer to read. In addition, the spot size can be adjusted to investigate the effect of the fluence, energy, and spotsize of the laser on the resulting splash.

Acknowledgements

I would like to thank all people involved in this project for the useful discussions, ready cooperation, and feedback. At ARCNL/AMOLF these people were: Oscar Versolato, Bo Liu, Laurens van Buuren, Henk-Jan Boluijt, and the entire plasma processes group. At the TU/e these people were: Jaap Hermens, Niek Lopes-Cardozo, and Peter Rindt.

References

[1] F. Rahman, "Extreme UV Sources Fill the Gap," May 2018.

[2] N. R. Böwering, "Performance results of laser-produced plasma test and prototype light sources for EUV lithography," *Journal of Micro/Nanolithography, MEMS, and MOEMS*, vol. 8, p. 041504, Oct. 2009.

[3] I. V. Fomenkov, A. A. Schafgans, Y. Tao, R. J. Rafac, M. Purvis, S. I. Rokitski, M. Kats, J. Stewart, A. D. LaForge, A. I. Ershov, C. Rajyaguru, G. O. Vaschenko, D. C. Brandt, D. J. Brown, M. Vargas, S. D. Rich, M. Mulder, E. Buurman, and M. Abraham, "Industrialization of a robust EUV source for high-volume manufacturing and power scaling beyond 250W," in *Extreme Ultraviolet (EUV) Lithography IX* (N. M. Felix and K. A. Goldberg, eds.), (San Jose, United States), p. 79, SPIE, May 2018.

[4] M. Sharbati, *Graphene Quantum Dot-Based Organic Light Emitting Diodes*. PhD thesis, Apr. 2016.

[5] R. S. Abhari, B. Rollinger, A. Z. Giovannini, O. Morris, I. Henderson, and S. S. Ellwi, "Laser-produced plasma light source for extreme-ultraviolet lithography applications," *Journal of Micro/Nanolithography, MEMS, and MOEMS*, vol. 11, pp. 021114–1, June 2012.

[6] S. Mirnov, "Plasma-wall interactions and plasma behaviour in fusion devices with liquid lithium plasma facing components," *Journal of Nuclear Materials*, vol. 390-391, pp. 876–885, June 2009.

[7] H. Kugel, J. Allain, M. Bell, R. Bell, A. Diallo, R. Ellis, S. Gerhardt, B. Heim, M. Jaworski, R. Kaita, J. Kallman, S. Kaye, B. LeBlanc, R. Maingi, A. McLean, J. Menard, D. Mueller, R. Nygren, M. Ono, S. Paul, R. Raman, A. Roquemore, S. Sabbagh, H. Schneider, C. Skinner, V. Soukhanovskii, C. Taylor, J. Timberlake, M. Viola, and L. Zakharov, "NSTX plasma operation with a Liquid Lithium Divertor," *Fusion Engineering and Design*, vol. 87, pp. 1724–1731, Oct. 2012.

[8] A. Vertkov, I. Lyublinski, M. Zharkov, G. Mazzitelli, M. Apicella, and M. Iafrati, "Liquid tin limiter for FTU tokamak," *Fusion Engineering and Design*, vol. 117, pp. 130–134, Apr. 2017.

[9] P. Rindt, N. Lopes Cardozo, J. van Dommelen, R. Kaita, and M. Jaworski, "Conceptual design of a pre-loaded liquid lithium divertor target for NSTX-U," *Fusion Engineering and Design*, vol. 112, pp. 204–212, Nov. 2016.

[10] T. Morgan, A. Vertkov, K. Bystrov, I. Lyublinski, J. Genuit, and G. Mazzitelli, "Power handling of a liquid-metal based CPS structure under high steady-state heat and particle fluxes," *Nuclear Materials and Energy*, vol. 12, pp. 210–215, Aug. 2017.

[11] M. Jaworski, T. Abrams, J. Allain, M. Bell, R. Bell, A. Diallo, T. Gray, S. Gerhardt, R. Kaita, H. Kugel, B. LeBlanc, R. Maingi, A. McLean, J. Menard, R. Nygren, M. Ono, M. Podesta, A. Roquemore, S. Sabbagh, F. Scotti, C. Skinner, V. Soukhanovskii, D. Stotler, and the NSTX Team, "Liquid lithium divertor characteristics and plasma–material interactions in NSTX high-performance plasmas," *Nuclear Fusion*, vol. 53, p. 083032, Aug. 2013.

[12] Y. Igitkhanov and B. Bazylev, "Modeling of DEMO PFC Erosion Due to ELM Impact," *IEEE TRANSACTIONS ON PLASMA SCIENCE*, vol. 42, no. 9, p. 7, 2014.

[13] S. Clara, "Operation and Maintenance Manual for Surelite Lasers," p. 112.

[14] Z. Levin and P. V. Hobbs, "Splashing of Water Drops on Solid and Wetted Surfaces: Hydrodynamics and Charge Separation," *Philosophical Transactions of the Royal Society A: Mathematical, Physical and Engineering Sciences*, vol. 269, pp. 555–585, May 1971.

[15] G. E. Cossali, A. Coghe, and M. Marengo, "The impact of a single drop on a wetted solid surface," *Experiments in Fluids*, vol. 22, pp. 463–472, Apr. 1997.

[16] G. Liang and I. Mudawar, "Review of mass and momentum interactions during drop impact on a liquid film," *International Journal of Heat and Mass Transfer*, vol. 101, pp. 577–599, Oct. 2016.

[17] A. L. Yarin and D. A. Weiss, "Impact of drops on solid surfaces: self-similar capillary waves, and splashing as a new type of kinematic discontinuity," *Journal of Fluid Mechanics*, vol. 283, pp. 141–173, Jan. 1995.

[18] R. L. Vander Wal, G. M. Berger, and S. D. Mozes, "Droplets splashing upon films of the same fluid of various depths," *Experiments in Fluids*, vol. 40, pp. 33–52, Jan. 2006.

[19] J.-h. Guo and X.-y. Wang, "Simulation of the Two Phase Flow of Droplet Impingement on Liquid Film by the Lattice Boltzmann Method," *Journal of Hydrodynamics*, vol. 24, pp. 292–297, Apr. 2012.

[20] I. V. Roisman and C. Tropea, "Impact of a drop onto a wetted wall: description of crown formation and propagation," *Journal of Fluid Mechanics*, vol. 472, pp. 373–397, Dec. 2002.

[21] A. Geppert, A. Terzis, G. Lamanna, M. Marengo, and B. Weigand, "A benchmark study for the crown-type splashing dynamics of one- and two-component droplet wall–film interactions," *Experiments in Fluids*, vol. 58, p. 172, Dec. 2017.

[22] A.-B. Wang and C.-C. Chen, "Splashing impact of a single drop onto very thin liquid films," *Physics of Fluids*, vol. 12, pp. 2155–2158, Sept. 2000.

[23] C. Tropea and M. Marengo, *The impact of drops on walls and films*, vol. 11 of *Multiphase Science and Technology*. Begel House Inc., 1999.

[24] O. G. Engel, "Initial Pressure, Initial Flow Velocity, and the Time Dependence of Crater Depth in Fluid Impacts," *Journal of Applied Physics*, vol. 38, pp. 3935–3940, Sept. 1967.

[25] M. Bussman, J. Mostaghimi, and S. Chandra, "On a three-dimensional volume tracking model of droplet impact," *Physics of Fluids*, vol. 11, Feb. 1999.

[26] Y. Hardalupas, A. Taylor, and J. Wilkins, "Experimental investigation of sub-millimetre droplet impingement on to spherical surfaces," *International Journal of Heat and Fluid Flow*, vol. 20, pp. 477–485, Oct. 1999.

[27] G. Liang, Y. Guo, Y. Yang, S. Guo, and S. Shen, "Special phenomena from a single liquid drop impact on wetted cylindrical surfaces," *Experimental Thermal and Fluid Science*, vol. 51, pp. 18–27, Nov. 2013.

[28] G. Liang, Y. Guo, Y. Yang, and S. Shen, "Liquid sheet behaviors during a drop impact on wetted cylindrical surfaces," *International Communications in Heat and Mass Transfer*, vol. 54, pp. 67–74, May 2014.

[29] K. Range and F. Feuillebois, "Influence of Surface Roughness on Liquid Drop Impact," *Journal of Colloid and Interface Science*, vol. 203, pp. 16–30, July 1998.

[30] R. N. Wenzel, "RESISTANCE OF SOLID SURFACES TO WETTING BY WATER," *Industrial & Engineering Chemistry*, vol. 28, pp. 988–994, Aug. 1936.

[31] A. B. D. Cassie and S. Baxter, "Wettability of porous surfaces," *Transactions of the Faraday Society*, vol. 40, p. 546, 1944.

[32] A. Warren and A. Nylund, "Oxidation of Tungsten and Tungsten Carbide in Dry and Humid Atmospheres," p. 9.

[33] R. R. Netz and D. Andelman, "Roughness-induced wetting," *Physical Review E*, vol. 55, pp. 687–700, Jan. 1997.

[34] R. Hebbar, A. Isloor, and A. Ismail, "Contact Angle Measurements," in *Membrane Characterization*, pp. 219–255, Elsevier, 2017.

[35] J. Kruth, M. Badrossamay, E. Yasa, J. Deckers, L. Thijs, and J. van Humbeeck, "Part and material properties in selective laser melting of metals," in *Part and material properties in selective laser melting of metals*, (Shanghai, China), SHANGHAI JIAO TONG UNIV PRESS, Apr. 2010.

[36] A. Iveković, N. Omidvari, B. Vrancken, K. Lietaert, L. Thijs, K. Vanmeensel, J. Vleugels, and J.-P. Kruth, "Selective laser melting of tungsten and tungsten alloys," *International Journal of Refractory Metals and Hard Materials*, vol. 72, pp. 27–32, Apr. 2018.

[37] H. H. Alsalla, C. Smith, and L. Hao, "Effect of build orientation on the surface quality, microstructure and mechanical properties of selective laser melting 316L stainless steel," *Rapid Prototyping Journal*, vol. 24, pp. 9–17, Jan. 2018.

[38] E. Yasa and J.-P. Kruth, "Microstructural investigation of Selective Laser Melting 316L stainless steel parts exposed to laser re-melting," *Procedia Engineering*, vol. 19, pp. 389–395, 2011.

[39] Z. Dong, Y. Liu, W. Wen, J. Ge, and J. Liang, "Effect of Hatch Spacing on Melt Pool and As-built Quality During Selective Laser Melting of Stainless Steel: Modeling and Experimental Approaches," *Materials*, vol. 12, p. 50, Dec. 2018.

[40] M. J. Assael, A. E. Kalyva, K. D. Antoniadis, R. Michael Banish, I. Egry, J. Wu, E. Kaschnitz, and W. A. Wakeham, "Reference Data for the Density and Viscosity of Liquid Copper and Liquid Tin," *Journal of Physical and Chemical Reference Data*, vol. 39, p. 033105, Sept. 2010.

[41] T. R. Hogness, "THE SURFACE TENSIONS AND DENSITIES OF LIQUID MERCURY, CADMIUM, ZINC, LEAD, TIN AND BISMUTH.," *Journal of the American Chemical Society*, vol. 43, pp. 1621–1628, July 1921.

[42] T. Hoar and D. Melford, "The surface tension of binary liquid mixtures: lead + tin and lead+indium alloys," Jan. 1957.

[43] E. Pelzel *Monatsch*, no. 94, p. 11, 1949.

[44] M. Kehr, W. Hoyer, and I. Egry, "A New High-Temperature Oscillating Cup Viscometer," *International Journal of Thermophysics*, vol. 28, pp. 1017–1025, Sept. 2007.

[45] R. Chhabra and D. Sheth, "Viscosity of molten metals and its temperature-dependence," *Zeitschrift fur Metallkunde*, vol. 81, no. 4, pp. 264–271, 1990.

[46] S. Kaufman and T. Whalen, "The surface tension of liquid gold, liquid tin, and liquid gold-tin binary solutions," *Acta Metallurgica*, vol. 13, pp. 797–805, July 1965.

[47] C. Mundo, M. Sommerfeld, and C. Tropea, "Droplet-wall collisions: Experimental studies of the deformation and breakup process," *International Journal of Multiphase Flow*, vol. 21, pp. 151–173, Apr. 1995.

[48] D. Kurilovich, M. M. Basko, D. A. Kim, F. Torretti, R. Schupp, J. C. Visschers, J. Scheers, R. Hoekstra, W. Ubachs, and O. O. Versolato, "Power-law scaling of plasma pressure on laser-ablated tin microdroplets," *Physics of Plasmas*, vol. 25, p. 012709, Jan. 2018.

[49] D. Kurilovich, A. L. Klein, F. Torretti, A. Lassise, R. Hoekstra, W. Ubachs, H. Gelderblom, and O. O. Versolato, "Plasma Propulsion of a Metallic Microdroplet and its Deformation upon Laser Impact," *Physical Review Applied*, vol. 6, p. 014018, July 2016.

[50] E. Villermaux, "Fragmentation," *Annual Review of Fluid Mechanics*, vol. 39, pp. 419–446, 2007.

[51] E. Villermaux and B. Bossa, "Drop fragmentation on impact," *Journal of Fluid Mechanics*, vol. 668, pp. 412–435, Feb. 2011.

[52] J. Gonzalo, C. N. Afonso, and J. Perrière, "Influence of laser energy density on the plasma expansion dynamics and film stoichiometry during laser ablation of BiSrCaCuO," *Journal of Applied Physics*, vol. 79, pp. 8042–8046, May 1996.

[53] P. Rindt, J. Mata González, P. Hoogerhuis, P. van den Bosch, M. van Maris, D. Terentyev, C. Yin, M. Wirtz, N. Lopes Cardozo, J. van Dommelen, and T. Morgan, "Using 3D-printed tungsten to optimize liquid metal divertor targets for flow and thermal stresses," *Nuclear Fusion*, vol. 59, p. 054001, May 2019.

[54] D. Liu and J. Yu, "Otsu Method and K-means," in *2009 Ninth International Conference on Hybrid Intelligent Systems*, (Shenyang, China), pp. 344–349, IEEE, 2009.

[55] M. H. J. Vala and A. Baxi, "A Review on Otsu Image Segmentation Algorithm," vol. 2, no. 2, p. 3.

[56] J. B. Blaisot and J. Yon, "Droplet size and morphology characterization for dense sprays by image processing: application to the Diesel spray," *Experiments in Fluids*, vol. 39, pp. 977–994, Dec. 2005.

[57] A. Bisighini, "Single and double drop impacts onto deep and thick liquid layers," p. 173.

11 Appendix

Splash images for 5mJ, 10mJ, and 20mJ

In figures 11.1-11.3 splash images for several times are given for the laser energies of 5mJ, 10mJ, and 20mJ respectively. To highlight the statistical nature of the data, 5 images are selected at random for times 30, 90, 150, and 240 µs after laser impact. Visible differences between the figures of varying laser energies are the droplet number and size at each time after impact.

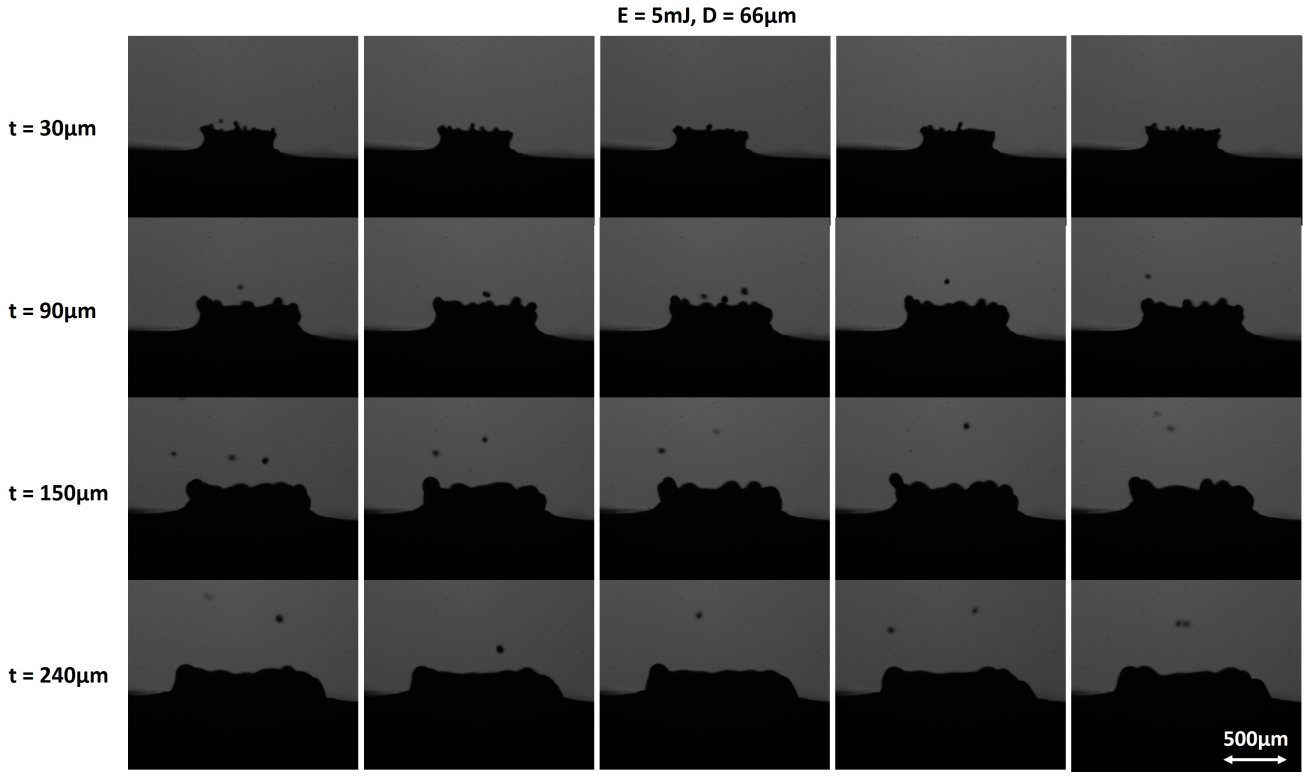

Figure 11.1: Data images from a laser impact splash. The laser energy is 5mJ, the spotsize of the laser is 66µm. *For* 30µs, 90µs, 150µs, *and* 240µs *five different images are given.*

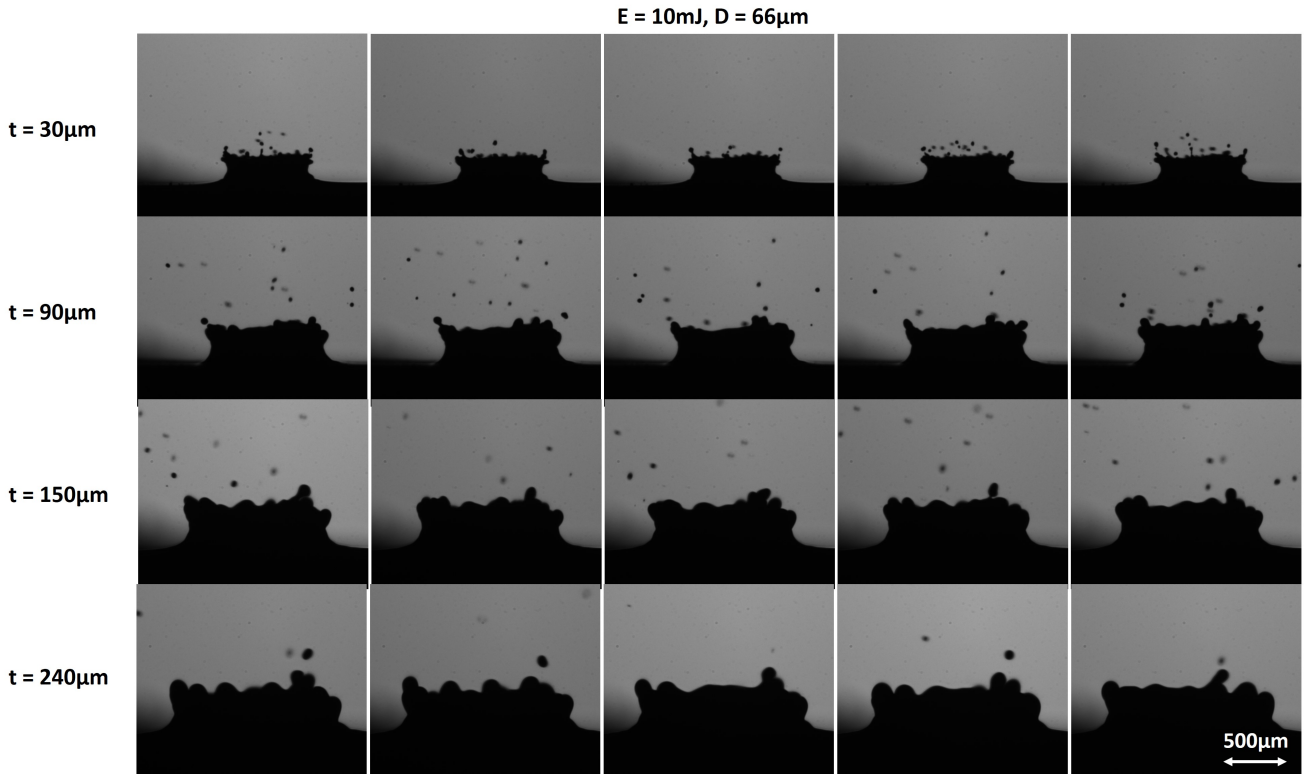

Figure 11.2: Data images from a laser impact splash. The laser energy is 10mJ, the spotsize of the laser is 66µm. *For* 30µs, 90µs, 150µs, *and* 240µs *five different images are given.*

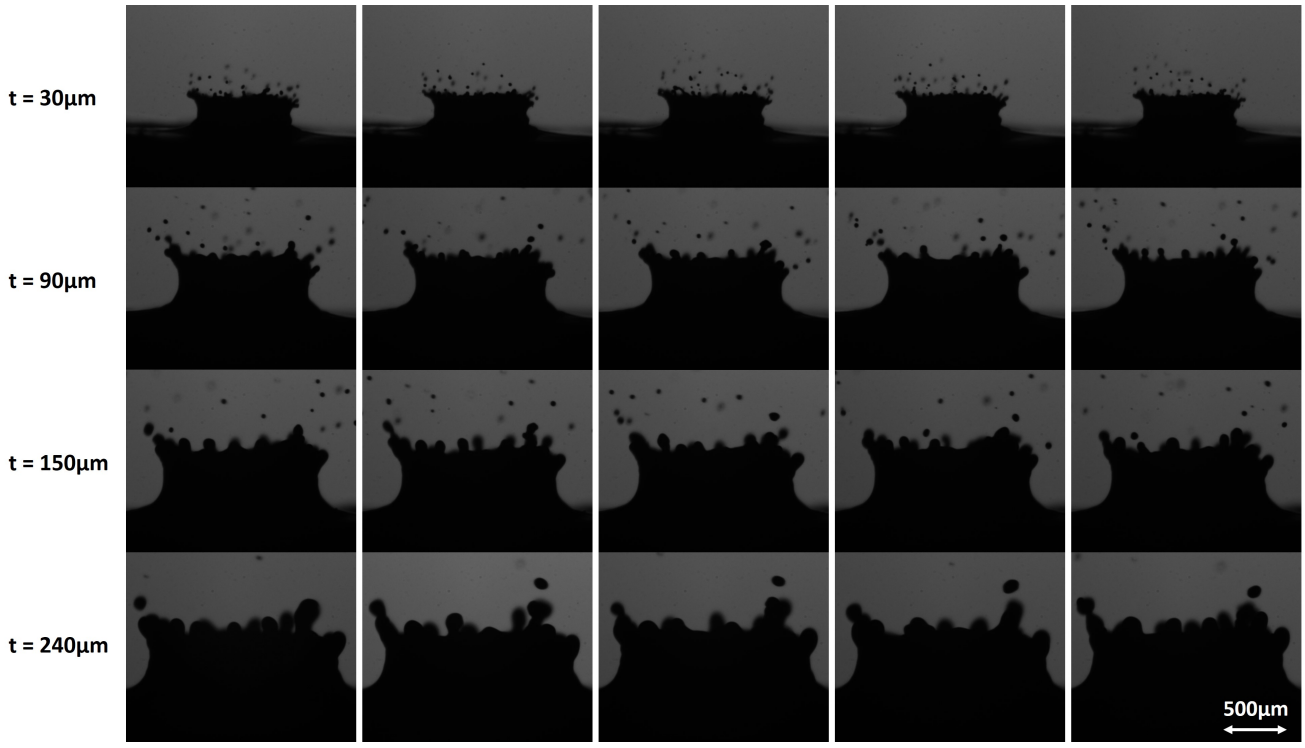

Figure 11.3: Data images from a laser impact splash. The laser energy is 20mJ, the spotsize of the laser is 66µm. *For* 30µs, 90µs, 150µs, *and* 240µs *five different images are given.*

List of Figures